2015

Z-Spectral Modeling for Magnetization Transfer Ratio Asymmetry Calculations in Chemical Exchange Saturation Transfer MRI at 3 Tesla

Ryan Nicholas Schurr
Louisiana State University and Agricultural and Mechanical College, rschur2@tigers.lsu.edu

Z-SPECTRAL MODELING FOR MAGNETIZATION TRANSFER RATIO ASYMMETRY CALCULATIONS IN CHEMICAL EXCHANGE SATURATION TRANSFER MRI AT 3 TESLA

A Thesis

Submitted to the Graduate Faculty of the
Louisiana State University and
Agricultural and Mechanical College
in partial fulfillment of the
requirements for the degree of
Master of Science

in

The Department of Physics and Astronomy

by
Ryan N. Schurr
B.S., Clemson University, 2012
August 2015

ACKNOWLEDGMENTS

I acknowledge the help and contributions of the many people who offered me assistance and guidance over the course of completing this project.

I thank Randy Deen and Kevin McKlveen, MR technologists at PBRC, for their time and assistance with data collection and sharing their knowledge of MRI. I thank Chenfei Gao, graduate student working at PBRC, for his assistance and guidance in building the phantom. I thank Dr. Jianhua Lu, post-doctoral researcher at LSU and PBRC, for sharing his knowledge of CEST-MRI with me.

I thank Saba Elias, physicist at The Ohio State University's Wexner Medical Center, for her willingness to give her assistance, knowledge, and time in scanning the phantom. I thank Danny Clark, M.D.-Ph.D. student at The Ohio State University for his time and assistance with scanning the phantom and helping me process the images.

I thank my advisor, Dr. Guang Jia, for sharing his energy, expertise, and knowledge of physics with me. His advice and guidance were invaluable and I am grateful for the opportunity to work with him. His always-positive attitude kept me encouraged throughout the course of the project.

I thank my committee members, Dr. Owen Carmichael, Dr. Kip Matthews, Dr. Joyoni Dey, and Dr. David Young, for offering their time and assistance and sharing their knowledge of physics and experimental design.

Additionally, I thank the entirety of the Medical Physics faculty for their invaluable instruction and guidance over the course of my entire education at LSU.

TABLE OF CONTENTS

LIST OF TABLES

LIST OF FIGURES

LIST OF ABBREVIATIONS

AICc – bias-corrected Akaike's Information Criterion

CEST – chemical exchange saturation transfer

CG – central gland

DWS – direct water saturation

FFE – fast field echo

FOV – field of view

HIPAA – Health Insurance Portability and Accountability Act

IDL – interactive data language

IRB – institutional review board

MT – magnetization transfer

MTR – magnetization transfer ratio

NBW – normal bladder wall

NEX – number of excitations

NMR – nuclear magnetic resonance

NOE – Nuclear Overhauser Effect

NSA – number of signal averages

PZ – peripheral zone

RF – radiofrequency

ROI – region of interest

TE – echo time

TR – repetition time

TSE – turbo spin echo

ABSTRACT

Chemical exchange saturation transfer (CEST) and magnetization transfer (MT) are types of magnetic resonance imaging (MRI) experiments in which contrast is based on the transfer of magnetization from selectively saturated solute or macromolecular protons to bulk water protons. These processes offer insight into the chemical composition of tissue and are quantified by the asymmetry of the magnetization transfer ratio (MTR_{asym}). This study was to develop a Z-spectral curve fitting procedure based on the underlying physics of CEST-MRI from which MTR_{asym} values can be calculated and applied to distinguish healthy tissue from cancer.

Z-spectra were collected from CEST-MR images of a phantom. The data were fit to both the proposed model which separately fits the upfield and downfield regions of the Z-spectra, and two polynomial models from literature. A preferred model was identified using the small sample bias-corrected Akaike's Information Criterion (AICc). Z-spectra were collected from CEST-MR images of prostate cancer patients and fit with the same models; the preferred model was selected using the AICc. CEST-MR images of bladder cancer patients were acquired and the Z-spectra were fit with the preferred model identified from the phantom images. MTR_{asym} was calculated at frequency offsets of 3.5 ppm and 2.0 ppm to determine if these quantities were capable of distinguishing normal bladder wall (NBW) from bladder cancer.

The proposed fitting model with a 5^{th} order polynomial for the downfield region was the preferred curve fitting model by the AICc model selection procedure for the phantom while a 6^{th} order polynomial was preferred for the prostate cancer Z-spectra. MTR_{asym}(2.0 ppm) values calculated from the bladder cancer Z-spectra did not differ significantly between the NBW and tumor regions. A statistically significant difference existed between the NBW and tumor regions for the MTR_{asym}(3.5 ppm) values ($p < 0.001$).

The proposed model was preferred to the polynomial models from literature based on the AICc metric. Application of the technique to patient images showed the potential to distinguish NBW from bladder cancer based on the statistically significant MTR_{asym}(3.5 ppm) values in these regions.

CHAPTER 1: INTRODUCTION

1.1 MRI PHYSICS REVIEW

1.1.1 NUCLEAR MAGNETIC RESONANCE

Some species of nuclei have an intrinsic magnetic moment, which will be oriented isotropically in a material under normal conditions. In the presence of a strong external magnetic field, these magnetic moments will align to either parallel (low energy) or antiparallel (high energy) states to create a net magnetic moment oriented in the direction of the external magnetic field (Figure 1.1). The ratio of the number of protons in the low energy state to the number of protons in the high energy state is determined by

$$\frac{n_{spin\ up}}{n_{spin\ down}} = e^{-\frac{\hbar\gamma B_0}{kT}} \tag{1.1}$$

where γ represents the gyromagnetic ratio (42.58 MHz/T for hydrogen nuclei), ħ is the Dirac constant (1.05×10^{-34} Js), k is the Boltzmann constant (1.38×10^{-23} $m^2kgs^{-2}K^{-1}$), T is the temperature (37˚C for the human body), and B_0 is the strength of the external magnetic field (Haacke, Brown et al. 1999). The gyromagnetic ratio, γ, is a property of the nucleus. For MR imaging of the human body, the hydrogen nucleus due to the large abundance of both water and fat in the human body (Westbrook, Roth et al. 2011).

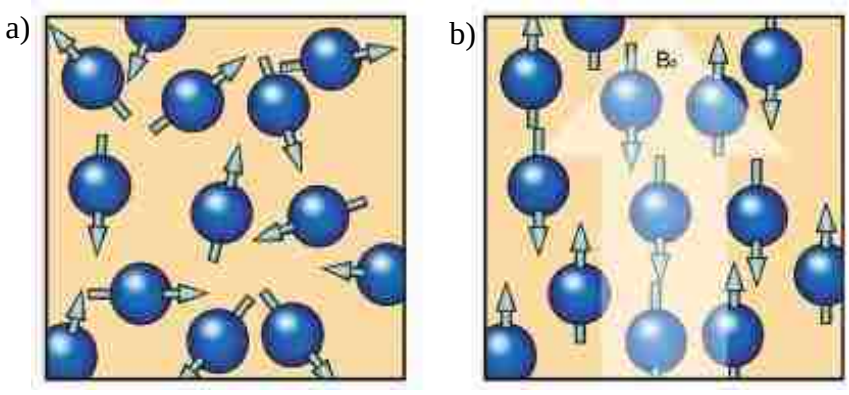

Figure 1.1: (a) Alignment of proton magnetic moments in the absence of a magnetic field, and (b) in the presence of a strong external magnetic field. Adapted from Westbrook 2011.

Although the net magnetic moment aligns with the external magnetic field, the magnetic moments of the individual hydrogen nuclei maintain an angle of 54.73˚ from the direction of the external magnetic field and precess about this field at the resonance or Larmor frequency, ω_0, given by

$$\omega_0 = \gamma B_0 \tag{1.2}$$

where γ is the gyromagnetic ratio and B_0 is the strength of the external magnetic field (Figure 1.2). For hydrogen nuclei in a 3 T external magnetic field, the Larmor frequency is 127.7 MHz.

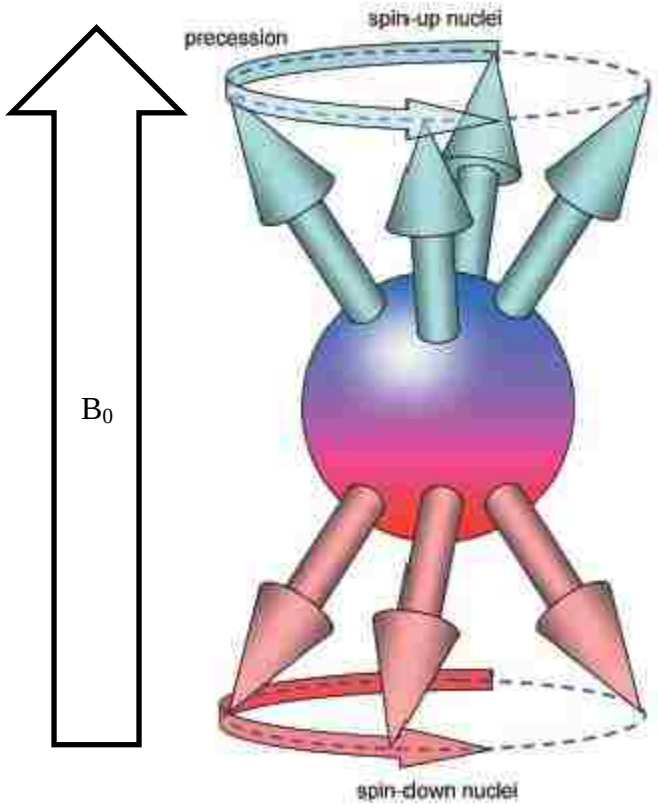

Figure 1.2: The precession of an individual magnetic moment about the direction of the external magnetic field. Adapted from Westbrook 2011.

1.1.2 CHEMICAL SHIFT

Though all nuclei of a single species have a constant gyromagnetic ratio, the resonance frequency of these nuclei can change based on the electronic environment. Changes in geometry

including bond length and bond angle, as well as the electronegativity of elements participating in a bond, affect the net magnetic field experienced by an individual nucleus. From Equation 1.2, a change in magnetic field strength changes the resonance frequency of the nucleus. This shift is often expressed in units of parts per million (ppm or Hz/MHz), calculated as

$$\Delta\omega = \frac{\omega - \omega_{ref}}{\omega_{ref}} \tag{1.3}$$

where ω is the resonance frequency of the shifted nucleus and ω_{ref} is the resonance frequency of a reference material. Tetramethylsilane (TMS) is commonly chosen as a reference material.

Due to the effect of chemical structure on the resonance frequency of nuclei, NMR spectroscopy is able to identify the types of bonds in a sample (Figure 1.3).

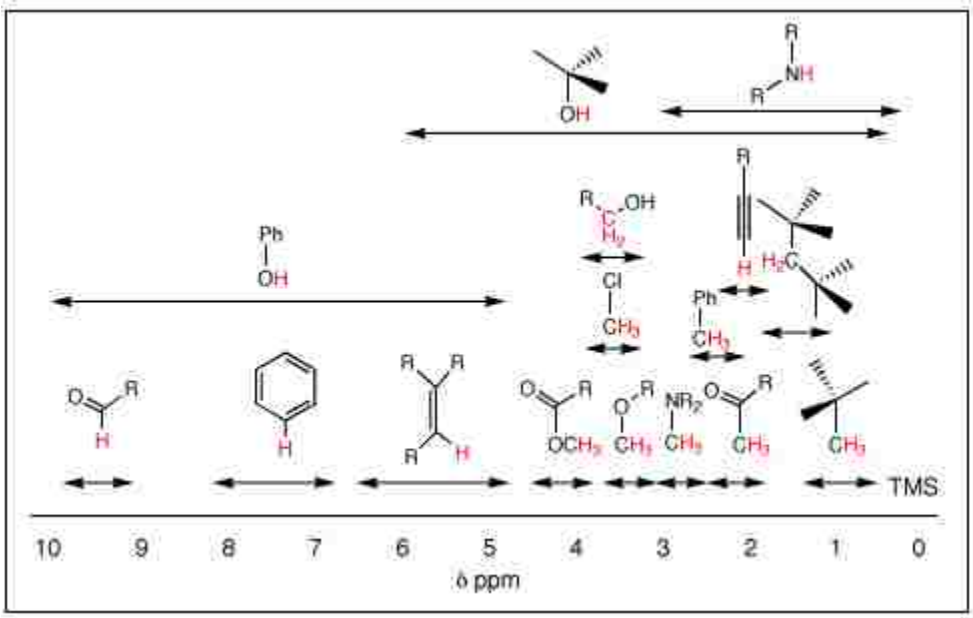

Figure 1.3: The amount of chemical shift varies depending on molecular structure and the electronegativity of participating atoms. Figure adapted from the University of Colorado's organic chemistry NMR theory tutorial (orgchem.colorado.edu).

1.1.3 MAGNETIC SUSCEPTIBILITY

Magnetic susceptibility is a property of a material that describes the relationship between the magnetization of the material and the strength of an applied external magnetic field, which

causes differences in the Larmor frequency of protons in the context of MRI. This change in Larmor frequency causes signal loss at the interface between materials with different magnetic susceptibilities, and the magnitude of the resulting artifact (Figure 1.4) can range from insignificant to severe; the presence of ferromagnetic materials especially causes B_0 field inhomogeneity in surrounding tissues.

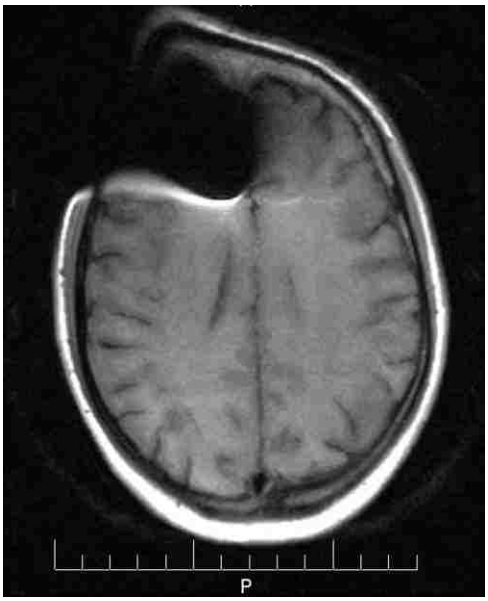

Figure 1.4: Magnetic susceptibility artifact due to a metallic substance located on the surface of the patient's skin. This case is courtesy of Dr. Ayush Goel of Radiopaedia.org.

The B_0 field inhomogeneities caused by differences in magnetic susceptibility between tissues and even in regions within a tissue also have an effect on chemical shift and MR spectroscopy. The resonance frequency of protons is shifted an amount based on the magnitude of the B_0 field inhomogeneity as described by the Larmor equation (Equation 1.2). The entire MR spectrum becomes shifted laterally along the frequency axis.

1.2 MAGNETIZATION TRANSFER

The T_2 relaxation time of protons associated with immobile macromolecules is too short for direct imaging with standard ^{1}H MRI (Henkelman, Stanisz et al. 2001). However, these

macromolecular protons can be detected indirectly based on the interactions with water protons. An off-resonance radiofrequency saturation pulse can selectively excite the macromolecular spins; the magnetization will subsequently be transferred to water protons (Figure 1.5) through a combination of spin-spin interactions and direct chemical exchange of protons. This magnetization transfer (MT) process is described using a two pool model, with one pool representing the water protons (bulk water pool or free pool) and the other representing the macromolecular protons (bound pool), each with their own relaxation rates and an exchange rate between the two pools (Figure 1.6). Though the goal of magnetization transfer MRI (MT-MRI) is to detect changes in the bulk water pool due to MT from the bound pool, some direct saturation of the water pool (direct water saturation, DWS) always occurs when the saturation pre-pulse is applied.

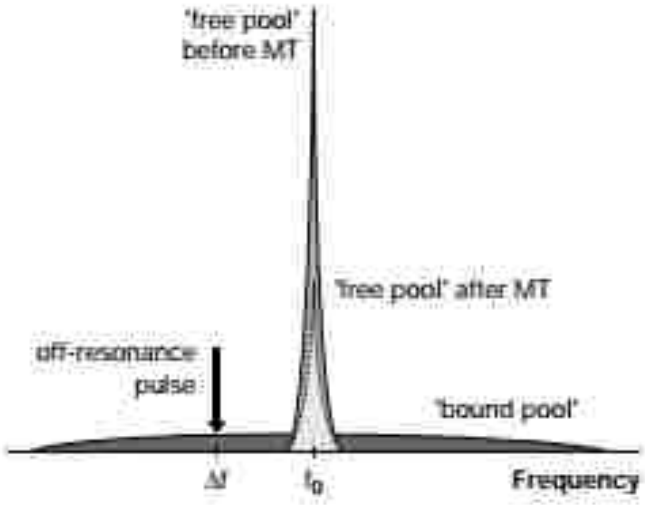

Figure 1.5: An off-resonance RF saturation pulse applied to the bound pool reduces the signal detected from the water pool following magnetization transfer. Adapted from Henkelman 2001.

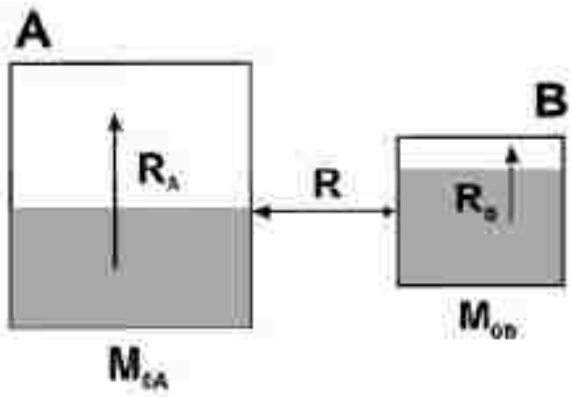

Figure 1.6: The larger pool (A) representing the water pool, and a smaller macromolecular pool (B). The exchange rate R describes the transfer of magnetization between the two pools. Adapted from Henkelman 2001.

The magnetizations of the two pools in this model are described by the Bloch equations, modified to include exchange terms:

$$\frac{dM_z^a}{dt} = R_a(M_0^a - M_z^a) - RM_0^bM_z^a + RM_0^aM_z^b + \omega_1 M_y^a \tag{1.4}$$

$$\frac{dM_z^b}{dt} = R_b\left(M_0^b - M_z^b\right) - RM_0^aM_z^b + RM_0^bM_z^a + \omega_1 M_y^b \tag{1.5}$$

$$\frac{dM_x^a}{dt} = -\frac{M_x^a}{T_{2a}} - 2\pi\Delta M_y^a \tag{1.6}$$

$$\frac{dM_x^b}{dt} = -\frac{M_x^b}{T_{2b}} - 2\pi\Delta M_y^b \tag{1.7}$$

$$\frac{dM_y^a}{dt} = -\frac{M_y^a}{T_{2a}} + 2\pi\Delta M_x^a - \omega_1 M_z^a \tag{1.8}$$

$$\frac{dM_y^b}{dt} = -\frac{M_y^b}{T_{2b}} + 2\pi\Delta M_x^b - \omega_1 M_z^b \tag{1.9}$$

where M_i^j represents the i^{th} component (x, y, or z) of the magnetization of the j^{th} pool (a = water and b = bound), R is the exchange rate, $R_{a,b}$ is the longitudinal relaxation rates of the water and bound pools (A and B), $M_0^{a,b}$ is the magnetization in the absence of saturation, Δ is the frequency offset of the RF saturation pulse (in Hz), $T_{2a,b}$ is the transverse relaxation times for the water (a) and bound (b) pools, and ω_1 is the angular frequency of precession caused by the RF saturation

pulse (Henkelman, Huang et al. 1993). Assuming steady state, these equations may be solved to provide a description of the magnetization of the water pool

$$M_Z^a = \frac{R_b\left(\frac{RM_0^b}{R_a}\right)+R_{rfb}+R_b+R}{\left(\frac{RM_0^b}{R_a}\right)(R_b+R_{rfb})+(1+\left(\frac{\omega_1}{2\pi\Delta}\right)^2\left(\frac{1}{R_aT_{2a}}\right)(R_b+R_{rfb}+R)} \quad (1.10)$$

where R_{rfb} is a function describing the RF absorption rate of the bound pool. While the solution of Equations 1.4-1.9 suggests a Lorentzian line shape for both the water and bound pools, experiments have shown a Gaussian function better fits the bound pool in agar, and a super-Lorentzian better fits the bound pool in tissue (Morrison and Henkelman 1995).

The imaging procedure for MT-MRI consists of a narrow-band RF saturation pre-pulse applied immediately prior to the image acquisition sequence (Figure 1.7). Common pulse sequences used to acquire these images include 2D single-slice fast spin echo or fast gradient echo techniques and 3D echo planar imaging techniques. In principle, the saturation pre-pulse can be applied prior to any image acquisition sequence, but in practice, fast imaging techniques are preferred to minimize the decay of the MT effect (Zaiss and Bachert 2013).

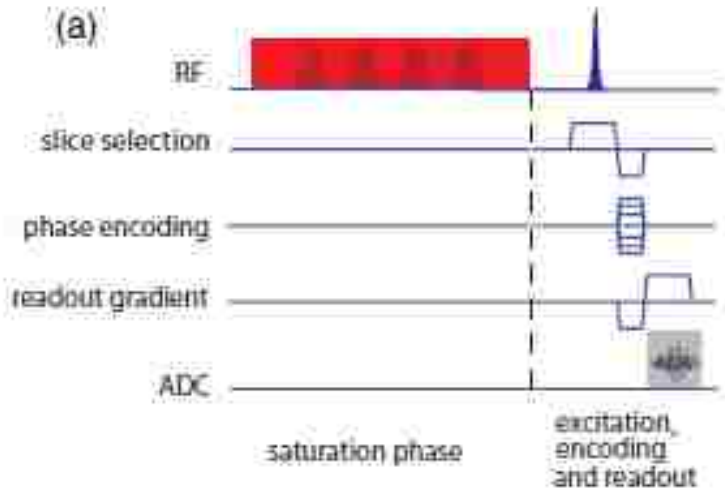

Figure 1.7: MT-MRI is performed by applying a RF saturation pre-pulse (red, left) prior to a standard imaging pulse sequence (right). Adapted from Zaiss 2013.

The effect of MT has been traditionally quantified by the magnetization transfer ratio, or MTR, which is calculated as:

$$MTR = 1 - \frac{S_{sat}}{S_0} \tag{1.11}$$

where S_{sat} is the signal intensity with the saturation pre-pulse and S_0 is the signal intensity in the absence of saturation.

Graphically, the effect of MT may be depicted by plotting signal intensity as a function of the frequency offset of the applied saturation pre-pulse (Figure 1.8). This often is called the Z-spectrum, or MT-spectrum (Bryant 1996). The plotted signal intensity is often normalized by the signal intensity in the absence of saturation, so the Z-spectrum may alternatively be thought of as the plot of 1-MTR versus the frequency offset of the applied saturation pre-pulse. However, for many MT-MRI experiments, the entire Z-spectrum need not be collected; a single image with the saturation pre-pulse applied at a sufficiently large frequency offset is often adequate for the purpose of MTR calculations (Kumar, Jagannathan et al. 2008).

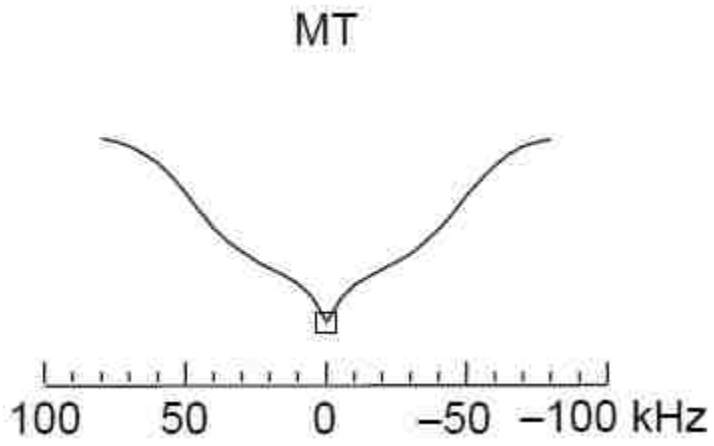

Figure 1.8: A hypothetical Z-spectrum for conventional MT from immobile macromolecules has a large width, with noticeable MT effects at saturation frequency offsets of 100 kHz. Adapted from Zhou 2006.

1.3 APPLICATIONS OF MAGNETIZATION TRANSFER MRI

MT-MRI has previously been applied to enhance contrast in MR angiography (Parker, Buswell et al. 1995) and brain imaging for multiple sclerosis (Mehta, Pike et al. 1995, Tozer, Ramani et al. 2003). Recently, quantitative MT-MRI has been utilized to detect the macromolecular protons in the prostate to distinguish cancer from healthy tissue (Arima, Hayashi et al. 1999, Kumar, Jagannathan et al. 2008, Kumar, Jagannathan et al. 2012), as prostate cancer tissues exhibit greater MT effects than healthy peripheral zone tissues based on the greater amount of relatively stationary structural tissue proteins and lipids (Riches 2009). MTR has recently been studied as a potential biomarker for bowel fibrosis (Pazahr, Blume et al. 2013, Martens, Lambregts et al. 2014). As of May 2015, there have been over 1700 publications on MT-MRI and over 400 publications on quantitative MT-MRI indexed in PubMed since 1988.

1.4 CHEMICAL EXCHANGE SATURATION TRANSFER

Chemical exchange saturation transfer (CEST) is a type of magnetization transfer where the decrease in water signal is due to the exchange of protons between solute molecules and water. Like MT from immobile macromolecules, CEST is most simply described using a two pool model with one pool representing the solute protons and the other pool representing the water protons. Unlike the protons associated with immobile macromolecules which have a broad RF absorption line shape that is approximately centered about water resonance, the solute protons have an RF absorption line shape that is narrow and asymmetric with respect to water resonance (Figure 1.9). The chemical shifts of some physiologically relevant types of solute protons are shown in Figure 1.10. (Zhou and van Zijl 2006)

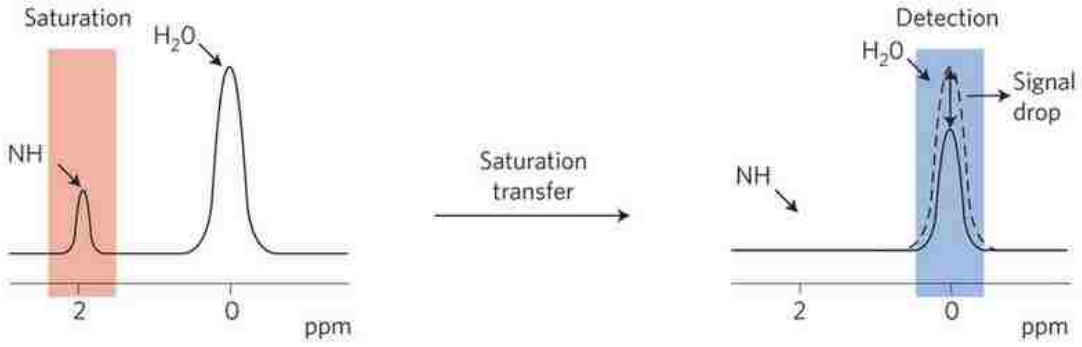

Figure 1.9: The RF absorption spectra of water and a NH solute pool (left) have a much narrower bandwidth than that of the broad macromolecular pool describing traditional magnetization transfer. Much like traditional MT, saturation is transferred to the water pool, reducing the amount of detectable water signal (right). Adapted from Ziv 2013.

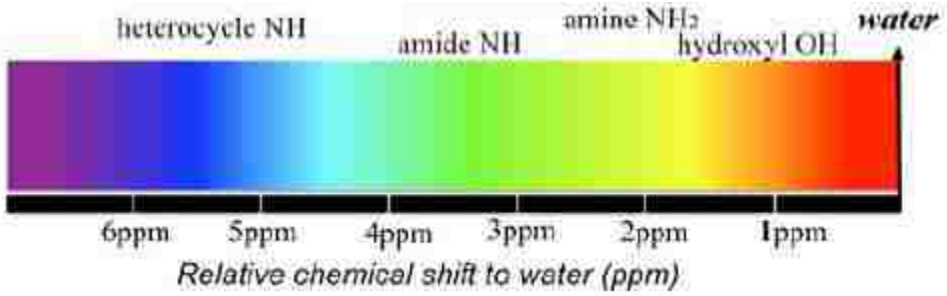

Figure 1.10: The chemical shifts of common solute protons for CEST-MRI *in vivo*. Adapted from Liu 2013.

Similar to magnetization transfer from immobile macromolecules, the magnetization of the water and solute pools may be described by modified versions of the Bloch equations which include exchange terms:

$$\frac{dM_x^s}{dt} = -\Delta\omega_s M_y^s - R_2^s M_x^s - k_{sw} M_x^s + k_{ws} M_x^w \tag{1.12}$$

$$\frac{dM_y^s}{dt} = \Delta\omega_s M_x^s + \omega_1 M_z^s - R_2^s M_y^s - k_{sw} M_y^s + k_{ws} M_y^w \tag{1.13}$$

$$\frac{dM_z^s}{dt} = -\omega_1 M_y^s - R_1^s (M_z^s - M_0^s) - k_{sw} M_z^s + k_{ws} M_z^w \tag{1.14}$$

$$\frac{dM_x^w}{dt} = -\Delta\omega_w M_y^w - R_2^w M_x^w + k_{sw} M_x^s - k_{ws} M_x^w \tag{1.15}$$

$$\frac{dM_y^w}{dt} = \Delta\omega_w M_x^w + \omega_1 M_z^w - R_2^w M_y^w + k_{sw} M_y^s - k_{ws} M_y^w \tag{1.16}$$

$$\frac{dM_z^w}{dt} = -\omega_1 M_y^w - R_1^w(M_z^w - M_0^w) + k_{sw}M_z^s - k_{ws}M_z^w \quad (1.17)$$

where M_i^j represent the i^{th} component (x, y, and z) of the magnetization of the j^{th} pool (s = solute, w = water); k_{sw} and k_{ws} represent the first order exchange rates from the solute pool to the water pool and the water pool to the solute pool, respectively; $\omega_1 = \gamma B_1$ where γ is the gyromagnetic ratio and B_1 is the magnitude of the applied RF saturation pulse; $\Delta\omega$ is defined as $\omega - \omega_0$ where ω is the location of the applied RF saturation field and $\omega_0 = \gamma B_0$ for external magnetic field strength B_0; and R_2 and R_1 are the transverse and longitudinal relaxation rates, respectively, of the water pool (w) and solute pool (s). These equations apply when the RF saturation pulse is applied along the x-direction. (Zhou, Wilson et al. 2004)

The imaging procedure for CEST-MRI is similar to the procedure for MT-MRI; an RF saturation pre-pulse is applied immediately prior to image acquisition. As with MT-MRI, fast imaging techniques such as echo planar imaging (EPI), fast spin echo, and fast gradient echo acquisitions are commonly used to minimize the decay of the transferred magnetization. Typically many images are acquired, covering a range of saturation frequency offsets. (Zaiss and Bachert 2013)

As with traditional MT, the CEST effect is displayed graphically as the Z-spectrum. The solute pools have narrow RF absorption spectra compared to the immobile macromolecules, which provide traditional MT, and the location of these absorption spectra near the water resonance introduces asymmetry to the Z-spectra (Figure 1.11a and b).

The CEST effect is described quantitatively as the asymmetry of the MTR with respect to water resonance (Figure 1.11c) at a particular offset frequency, $MTR_{asym}(\omega)$, which is defined as:

$$MTR_{asym}(\omega) = \frac{S_{sat}(-\omega) - S_{sat}(+\omega)}{S_0} \quad (1.18)$$

where $S_{sat}(-\omega)$ is the signal intensity with the saturation pulse applied at a frequency offset of –ω, $S_{sat}(+\omega)$ is the signal intensity with the saturation pulse applied at a frequency offset of +ω, and S_0 is the signal intensity in the absence of saturation (Zaiss and Bachert 2013). Another commonly used method of quantifying the CEST effect is the CEST ratio or CESTR, which is defined as:

$$CESTR(\omega) = \frac{S_{sat}(-\omega) - S_{sat}(+\omega)}{S_{sat}(-\omega)} \tag{1.19}$$

The analysis of asymmetry is based on the assumption that the only two factors contributing to the Z-spectrum are DWS and the CEST effect; by calculating asymmetry under these conditions, the DWS contribution to the MTR is removed.

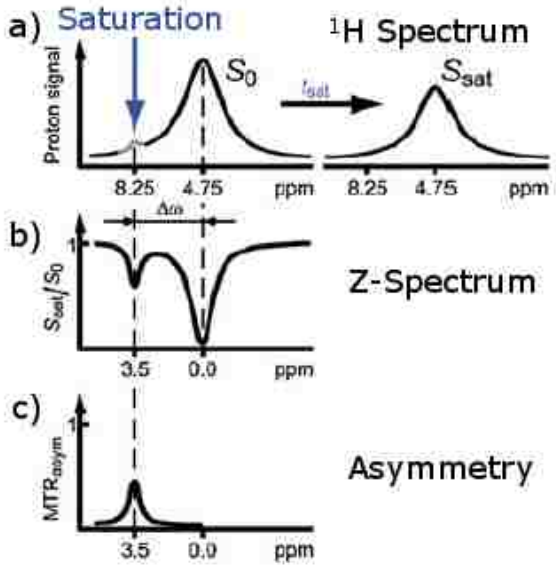

Figure 1.11: (a) The ^{1}H spectrum, showing a peak for the water pool and smaller solute pool, which disappears after saturation and (b) the resulting Z-spectrum, with an apparent asymmetry at the location of the solute pool. (c) CEST-MRI is quantitatively analyzed by calculating the asymmetry of the Z-spectrum. Adapted from Liu 2013.

Alternatively, one study investigated removing the DWS contribution through Fourier transform analysis in a technique called time domain removal of irrelevant magnetization (TRIM) rather than calculating MTR asymmetry (Yadav, Chan et al. 2013). In this technique, the

MTR as a function of saturation frequency offset is Fourier transformed into the time domain, where the signal is fit to a combination of three Lorentzian functions. The portion corresponding to DWS is removed from the time domain signal and transformed back into the frequency domain, yielding a measure of MTR with the contribution from DWS removed.

1.5 APPLICATIONS OF CHEMICAL EXCHANGE SATURATION TRANSFER MRI

The unique contrast mechanism provided by CEST-MRI has a number of potential applications, including distinguishing tumor from healthy tissue (Jia, Abaza et al. 2011), monitoring change in creatine concentration in skeletal muscle following exercise (Kogan, Haris et al. 2014), imaging cartilage based on chemical exchange between glycosaminoglycans and water (Singh, Haris et al. 2012), and monitoring breast cancer response to chemotherapy (Dula, Arlinghaus et al. 2013). Studies have demonstrated an increased CEST effect in brain tumors, and have applied CEST-MRI to distinguish peritumoral edema from white matter and to differentiate orthotopic gliomas from radiation induced necrosis (Kogan, Hariharan et al. 2013). As of May 2015, there have been 351 publications on CEST-MRI indexed in PubMed.

1.6 EXTERNAL MAGNETIC FIELD INHOMOGENEITY

The B_0 field inhomogeneity produced by differences in magnetic susceptibility (Section 1.1.3) shifts MR spectra along the frequency axis, causing the Z-spectrum to shift equivalently along the saturation offset frequency axis. In the case of CEST-MRI where the measurements of Z-spectral asymmetry are of interest, even small shifts in the positions of Z-spectra can result in large changes in asymmetry calculations, rendering them inaccurate unless a B_0 inhomogeneity correction is applied. Because B_0 field inhomogeneity laterally shifts the Z-spectrum by an amount proportional to $\gamma\Delta B$, the effect can be removed if the magnitude of the B_0 field inhomogeneity is known (Kim, Gillen et al. 2009).

A number of procedures for correcting B_0 field inhomogeneity have been demonstrated. For sufficiently separated CEST and direct water saturation (DWS) effects, a simple polynomial or spline fit is often applied and the minimum of the resulting fit assumed to be the center of the Z-spectrum for asymmetry calculations (Zhou, Payen et al. 2003). Another method uses B_0 field inhomogeneity maps acquired with an appropriate MR acquisition sequence to shift the Z-spectra; using a gradient echo acquisition with two different echo times, the magnitude of the B_0 field inhomogeneity, ΔB_0, is determined from the phase difference between the two images, as

$$\Delta B = \frac{\phi(TE_1) - \phi(TE_2)}{\gamma(TE_2 - TE_1)} \tag{1.20}$$

where γ is the gyromagnetic ratio of the proton, TE_i are the echo times, and the ϕ are the accumulated phases at each echo time (Haacke, Brown et al. 1999). This procedure has been applied to glycosaminoglycan CEST imaging (Wei, Jia et al. 2014). A technique known as water saturation shift referencing (WASSR), determines the magnitude of the B_0 field inhomogeneity effect by collecting a pure DWS image (Kim, Gillen et al. 2009). This is accomplished by applying a sufficiently weak RF saturation pre-pulse to minimize interference from both MT and CEST effects. Since the resulting DWS is symmetric, the center frequency can be determined by reflecting the Z-spectrum about 0 ppm and minimizing the difference between the acquired and reflected Z-spectra.

The points of interest on the Z-spectra for calculating MTR asymmetry are determined by the material exhibiting the CEST effect. The Z-spectra are collected at discrete frequency offsets, however; MTR asymmetry analysis is performed as a post-processing procedure. After B_0 field inhomogeneity correction is, the discrete Z-spectral data must be interpolated to calculate the MTR asymmetry values. Interpolation is commonly performed by fitting the Z-spectral data with

high order polynomials (Jia, Abaza et al. 2011). Other studies have investigated fitting with multiple Lorentzian functions with interaction cross-terms for multiple solute pools (Sun 2010).

1.7 PROSTATE CANCER AND MRI

In the United States, one in seven men is expected to develop prostate cancer during their lifetimes. In 2015, there will be an estimated 220,800 new cases of prostate cancer and more than 27,500 related deaths, accounting for more than 25% of cancer incidences and 8.8% of cancer related deaths in men (Siegel, Miller et al. 2015).

MRI often aids in the diagnosis and management of prostate cancer. Currently, multi-parametric techniques are used including T_1- and T_2- weighted MRI, diffusion weighted MRI, dynamic contrast-enhanced MRI, and MR spectroscopic imaging (Langer, van der Kwast et al. 2009, Hoeks, Barentsz et al. 2011).

1.8 BLADDER CANCER AND MRI

There are expected to be 74,000 new cases of bladder cancer and 16,000 related deaths in the United States in 2015. Bladder cancer is three times more common in men than in women, and is expected to account for 7% of all cancers in men and 4% of cancer deaths in men (Siegel, Miller et al. 2015).

Multi-parametric MRI techniques are often performed to aid in the management of bladder cancer. Contrast enhanced and diffusion weighted MRI have demonstrated the ability to identify muscle invasion with high accuracy (Green, Durand et al. 2012). These techniques also may find applications in evaluating and predicting response to chemotherapy (Nguyen, Jia et al. 2015).

1.9 MOTIVATION FOR RESEARCH

Currently, CEST-MRI has no universally applied method of data analysis. Z-spectral data are interpolated following B_0 correction using a variety of methods. This lack of standard procedure hinders comparison of results across multiple sites and studies, limiting the adoption of MTR_{asym} calculations as a clinically relevant quantitative imaging biomarker. Additionally, no standard CEST-MRI phantoms exist to assess the performance of analysis procedures and acquisition pulse sequences. The goal of this work was to evaluate curve fitting methods for Z-spectral data analysis that are based to varying degrees on the physics of CEST-MRI. Additionally, this work is to demonstrate the capability of MTR_{asym} calculations based on a selected model to distinguish tumor from healthy tissue.

1.10 HYPOTHESIS AND SPECIFIC AIMS

The hypothesis of this work was that independently fitting the upfield and downfield components of the Z-spectrum with a partially physics-based model will be preferred to fitting with high order polynomials based on the quality of fit. Quality of fit was assessed with both phantom and prostate MR images. The best quality method was used to calculate MTR_{asym} values.

Aim 1: Compare the quality of fits between a separate upfield and downfield fitting procedure and high order polynomial fitting procedure for a CEST-MRI phantom. A CEST-MRI phantom was designed, built, and imaged. Z-spectral data were extracted from these images and fit using a method with separate upfield and downfield components, as well as two high order polynomial models. The small sample bias-corrected Akaike's Information Criterion (AICc) was calculated for each fitting procedure and used to identify a preferred method of curve fitting for the phantom images.

Aim 2: Compare the quality of fits between the separate upfield and downfield fitting model and high order polynomial fitting models for CEST-MRI images of prostate cancer patients. Z-spectral data were extracted from images of prostate cancer patients in different regions of the prostate. The Z-spectral data were fit with a subset of the models tested in Aim 1. The quality of these fits was compared using the small sample bias-corrected AICc, identifying a preferred method of curve fitting for the patient images.

Aim 3: Apply the model to images of bladder cancer patients, and calculate the MTR_{asym} values to demonstrate capability of the model. Z-spectral data were extracted from images of bladder cancer patients and fit using the preferred method of curve fitting identified in Aims 1 and 2. The Z-spectral fits were used to calculate MTR_{asym} values in the different regions of the phantom to demonstrate that the measures of MTR_{asym} have the ability to distinguish bladder cancer from normal bladder tissue.

1.11 OVERVIEW OF THE THESIS

The specific aims were used to demonstrate the efficacy of separately fitting the Z-spectral components upfield and downfield from water resonance. Specifically, a preferred method of curve fitting was identified using the AICc for both phantom images and prostate cancer patient images, and this preferred method was applied to bladder cancer patient images to demonstrate the utility of the preferred model.

Chapter 2 explains the methods and procedures used to test the hypothesis that fitting the upfield and downfield components of the Z-spectra separately is preferable to fitting with a high order polynomial, based on a combination of parametric parsimony and discrepancy between the Z-spectral data and the fitting model. These methods and procedures include details regarding the design and construction of the phantom, as well as the prostate cancer patient imaging

technique. Chapter 2 also details the procedure of demonstrating the utility of the model by distinguishing healthy bladder tissue from tumor with these measurements.

Chapter 3 details the results of phantom development as well as comparison of fitting models. The preferred model for Z-spectral fitting was identified from the phantom study and the retrospective patient study. Additionally, MTR_{asym} measurements made using the preferred model were applied to assess their ability to distinguish bladder cancer from healthy bladder tissue.

Chapter 4 discusses the results, including the strengths and limitations of this work. This chapter also includes a recommendation for future research directions based upon the outcomes presented here.

CHAPTER 2: MATERIALS AND METHODS

2.1 Z-SPECTRAL CURVE FITTING METHOD – OVERVIEW

This study proposed a model which separately fits the upfield and downfield components of the Z-spectra obtained in CEST-MRI experiments (Figure 2.1). The effects of DWS, MT, and the Nuclear Overhauser Effect (NOE) are observed in the region of the Z-spectrum upfield from water resonance. The effects of DWS, MT, and CEST are expected to be observed in the downfield region of the Z-spectrum.

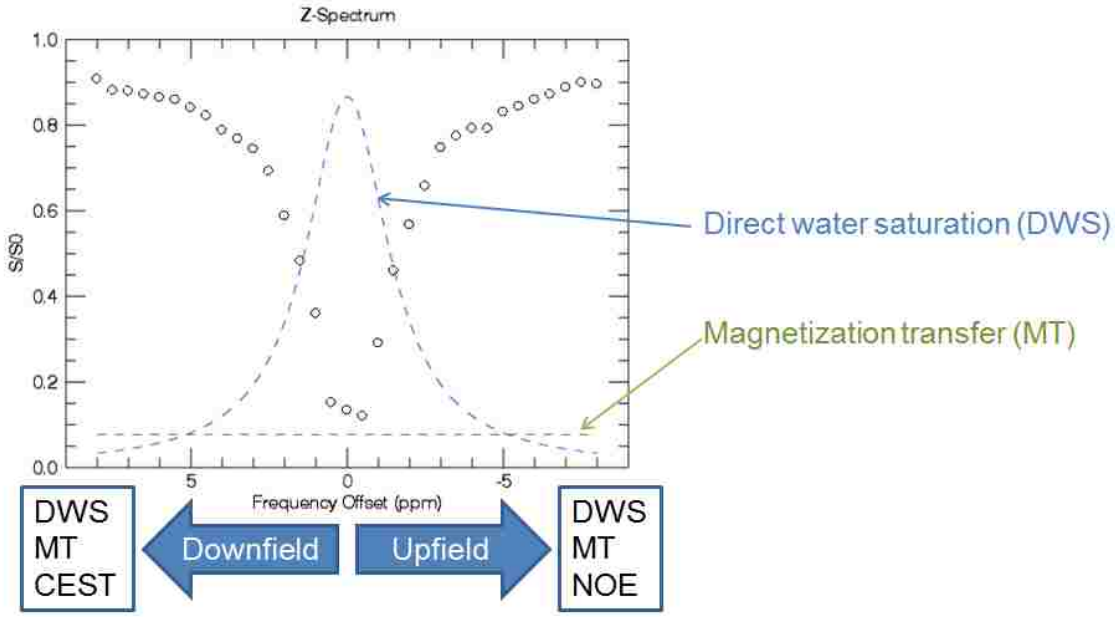

Figure 2.1: A sample Z-spectrum (open circles). Downfield from water, DWS, MT, and CEST effects are expected, while upfield from water DWS, MT, and NOE effects are expected. The DWS and MT components of this Z-spectrum are plotted and labeled.

The contribution from NOE is usually neglected in CEST-MRI measurements performed at a field strength of 3 T, although it can become significant at higher field strengths; a term can be added to account for NOW. NOE was not included in this work. A Lorentzian function was used to describe DWS (Zaiß, Schmitt et al. 2011), and a function was chosen for MT depending upon the material (Sections 2.1.1 and 2.1.2).

The downfield component of the Z-spectrum could potentially be modeled based on the different effects which are present, similar to the upfield component. For instance, using a sum of Lorentzian functions describing different solute pools with exchange terms could describe the downfield component, including the CEST contribution (Sun 2010). In tissue, however, the many different types of solute protons have overlapping regions of RF absorption, resulting in an excessive number of fitting parameters relative to the available number of data points. To avoid this, a polynomial was used to fit the downfield component.

These models combining the upfield and downfield components were referred to as the "combination model" in this work. The models were identified by the order of polynomial used to fit the downfield region of the Z-spectrum. For example, "6th order combination" would refer to fitting the upfield region with the DWS and MT components (see Equation 2.1 or Equation 2.2) and the downfield region with a 6th order polynomial.

2.1.1 Z-SPECTRAL CURVE FITTING METHOD - PHANTOM

Previous studies demonstrated that Gaussian functions appropriately describe the MT effect in agar (Morrison and Henkelman 1995). In Aim 1, MT in the phantom was provided by agar, so the upfield components of the Z-spectra was fit to:

$$\frac{S}{S_0} = 1 - \frac{A_w\left(\frac{G_w}{2}\right)^2}{\left(\frac{G_w}{2}\right)^2 + \Delta\omega^2} - A_b \exp\left[-\left(\frac{1}{2}\right)\left(\frac{\Delta\omega}{C_b}\right)^2\right] \quad (2.1)$$

where A_w and G_w were the magnitude and full width at half maximum (FWHM), respectively, of the Lorentzian describing DWS, $\Delta\omega$ was the frequency offset from water resonance, A_b was the magnitude of MT, and C_b was a constant, determined through curve fitting, describing the width of the Gaussian function used to describe MT in agar.

The downfield region was fit to polynomial functions, the orders of which are discussed in Section 2.3.5.

2.1.2 Z-SPECTRAL CURVE FITTING METHOD - PATIENT

Although it has been demonstrated that super-Lorentzian functions are a good description of MT in tissue, they are very broad relative to DWS and may be treated as constants in a small range near water resonance. In Aims 2 and 3, MT is provided by the relatively immobile macromolecules in tissue, so the upfield components of the Z-spectra were fit to:

$$\frac{S}{S_0} = 1 - \frac{A_w\left(\frac{G_w}{2}\right)^2}{\left(\frac{G_w}{2}\right)^2 + \Delta\omega^2} - A_b \tag{2.2}$$

where A_w and G_w were the magnitude and FWHM, respectively, of the Lorentzian describing DWS, $\Delta\omega$ was the frequency offset from water resonance, and A_b was the magnitude of MT.

2.2 MODEL SELECTION CRITERIA

The preferred fitting model was identified using the small sample bias-corrected Akaike Information Criterion (AICc). The AICc compares the quality of proposed fitting models for a set of data, with the preferred model having the most negative AICc value (Hurvich and Tsai 1989). The AICc is calculated based on the residual sum of squares (RSS), the sample size (n), and the number of fitting parameters in the proposed model (m), according to the equation:

$$AICc = n\ \ln\left(\frac{RSS}{n}\right) + n\frac{1+m/n}{1-(m+2)/n} \tag{2.3}$$

The AICc value was computed in IDL (Version 8.2, Exelis Visual Information Solutions) for each of the models tested following the curve fitting procedure. A pairwise Student's *t*-test was performed in the statistical analysis software R (Version 3.1.0, R Development Core Team) to determine if the average AICc values were statistically significantly different for the models. The preferred model will be identified as having the most negative average AICc; in cases where two models did not have significantly different average AICc values, the most negative maximum AICc was used.

2.3 AIM 1, APPLICATION OF MODEL TO CEST-MRI PHANTOM IMAGES

2.3.1 PHANTOM MATERIAL SELECTION

To create a CEST-MRI phantom, materials were selected with RF absorption covering a range of offset frequencies. The materials and their offset frequencies are listed in Table 2.1. All of the materials were incorporated in 2% agar to provide a broad MT effect due to immobile macromolecules, allowing the phantom to exhibit CEST effects in the presence of MT to mimic the situation that would be seen *in vivo*. Additionally, the agar was prepared with 0.01 M phosphate-buffered saline (PBS) with a pH of 7.4 to represent physiological. Three concentrations (Table 2.1) were selected for each material, either to match concentrations that have been used previously in literature or to use concentrations that are representative of physiological conditions.

Table 2.1: Concentrations of materials included in the CEST-MRI phantom and the corresponding frequency offset at which the CEST effects are expected.

	Material[ref]	Concentration A [mM]	Concentration B [mM]	Concentration C [mM]	Frequency Offset [ppm]
1	*Glycogen[1,2]	10	50	100	1.2
2	*Glucose[2]	10	50	100	1.3 - 2
3	*Creatine[3]	10	25	50	1.8
4	*L-Lysine[4]	1	10	100	3.0
5	*NH_4Cl[5]	100	500	1000	2.4
6	*Choline[6]	5	15	50	1.0
7	Agar[5]	2%	4%	6%	MT

* indicates the material was mixed in 2% agar.
1 Taylor 1996
2 van Zijl 2007
3 Kogan 2014
4 Ward 2000
5 Desmond 2012
6 Chen 2006

2.3.2 PHANTOM DEVELOPMENT

The selected materials were built into an existing MRI phantom (model MRI-R01, Data Spectrum Corporation, Durham, NC, USA). This cylindrical, water-filled phantom (Figure 2.2)

included plastic inserts which held twenty-one vials of 30 mL total volume each. The vials were separated into three groups of seven, shown in Figure 2.2 (right) and Figure 2.3.

Figure 2.2: The Data Spectrum Corporation's MRI phantom. The phantom includes inserts for spatial resolution, slice thickness, slice profile, linearity, and quantitative imaging (left), though only the quantitative imaging insert (right) is of interest to this study.

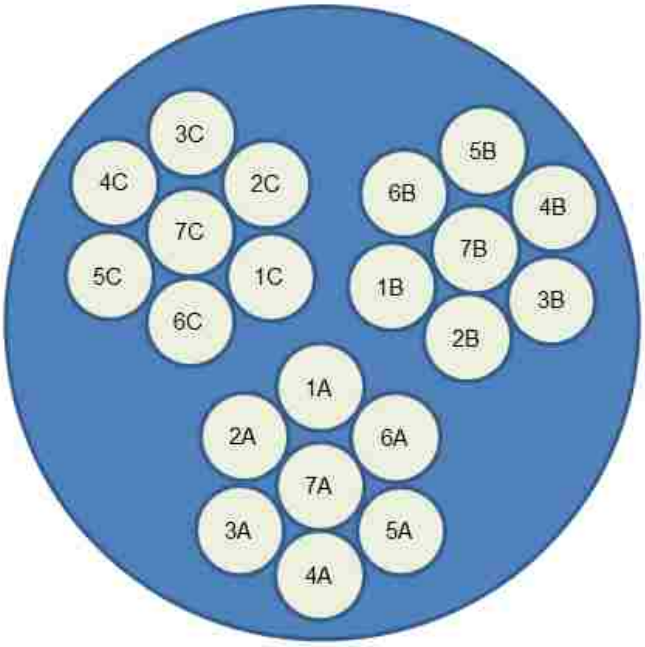

Figure 2.3: The layout of vials in the CEST phantom. Numbers 1-6 correspond to the materials as numbered in Table 2.1, while the letters A, B, and C identify the low concentrations, intermediate concentrations, and high concentrations, respectively. Vial 7 in each group contained agar alone in concentrations of 2% (7A), 4% (7B), or 6% (7C).

Each group of vials contained all six of the materials; one group was the lowest concentrations, one was the intermediate concentrations, and one was the highest concentrations. In each group, the vial closest to the central axis of the phantom was glycogen, with the remaining materials placed counterclockwise in the order of glucose, creatine, L-lysine, NH_4Cl, and choline (Figure 2.3). The central vial of each group contained the agar with a concentration of 2%, 4%, or 6%; the relative concentrations corresponded to the relative material concentrations, so that the groups could be identified by the magnitude of the MT effect in the agar vials.

The vials were glass liquid scintillation vials. The vials were filled with 0.36 g of powdered agar, 0.11 g of 5% w/v NaN_3 as an antibacterial agent (Hattori, Ikemoto et al. 2013), and the required mass of material to meet the concentrations listed in Table 2.1. These were mixed in PBS to a final mass of 18 g. Each mixture was heated in a water bath at 90°C for 20 minutes; the mixture was stirred halfway through the heating period. After heating, the mixtures were stirred again; the vials were capped and placed on ice to solidify.

2.3.3 PHANTOM IMAGING PROCEDURE

T_1-weighted and T_2-weighted images were acquired to assess the properties of the phantom. The images were acquired using a 4 channel head coil on a 3 T MR system (Signa, GE Healthcare, Waukesha, WI). T_1 mapping was performed using an inversion recovery technique. Images were acquired with a fast spin echo pulse sequence with the following sequence parameters: a TE of 15 ms; a TR of 7500 ms; multiple TIs of 1900 ms, 1600 ms, 1300 ms, 800 ms, 600 ms, and 500 ms; an echo train length of 16; receiver bandwidth of 50 kHz; a FOV of 30 × 30 cm^2; a slice thickness of 10 mm; a NEX of 1; acquisition matrix of 256 × 256; and the frequency encoding direction R/L. Post-processing for the T_1 map was performed using the

MRMap software (Version 1.4, Daniel Messroghli) written in IDL (Figure 2.4) and freely available for download online (http://sourceforge.net/projects/mrmap/).

T_2 measurements were made using a multiple echo time technique from images acquired with a fast spin echo pulse sequence with the following sequence parameters: TEs of 7.3 ms, 14.2 ms, 21.3 ms, 28.5 ms, 35.6 ms, 42.7 ms, 49.8 ms, and 56.9 ms; a TR of 1650 ms; a receiver bandwidth of 62.25 kHz; a FOV of 30 × 30 cm^2; a NEX of 1; an acquisition matrix of 320 × 256; and a frequency encoding direction of R/L. Post-processing for the T_2 calculations was performed using the Dynamic Magnetic Resonance Imaging Software Tool (Version OSU-5.0, Division of Imaging Research, The Ohio State University) written in IDL (Figure 2.5).

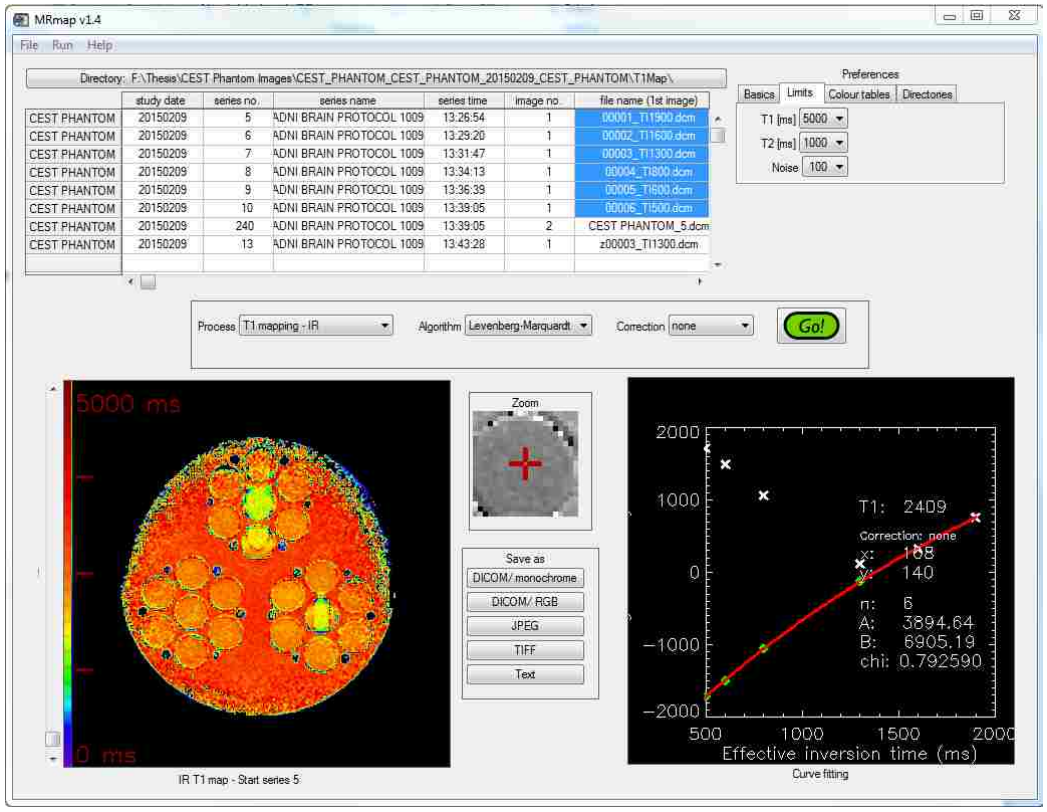

Figure 2.4: The software MRMap (Version 1.4, Daniel Messroghli) was used to create T_1 maps, performing the required curve fitting for each pixel.

For CEST-MR imaging, the phantom was imaged on a 3 T MR system (Achieva, Philips Healthcare, Cleveland, OH) using a 32 channel digital head coil. Images were acquired using a

2D multiple-shot turbo spin echo sequence (msTSE) with a TR of 3000 ms, TE of 26 ms, slice thickness of 6 mm, acquisition matrix size of 112 × 100, field of view of 225 × 225 mm^2, TSE factor of 20, NSA of 1, and flip angle of 90˚. A train of RF saturation pre-pulses consisting of 16 block pulses each 29 ms in length was applied at frequency offsets from 8 ppm to -8 ppm in 0.5 ppm increments. An additional image was acquired without saturation as a reference. A set of CEST-MR images was acquired for each of the following saturation amplitudes: 1.6 μT, 2.4 μT, 3.2 μT, and 4.0 μT.

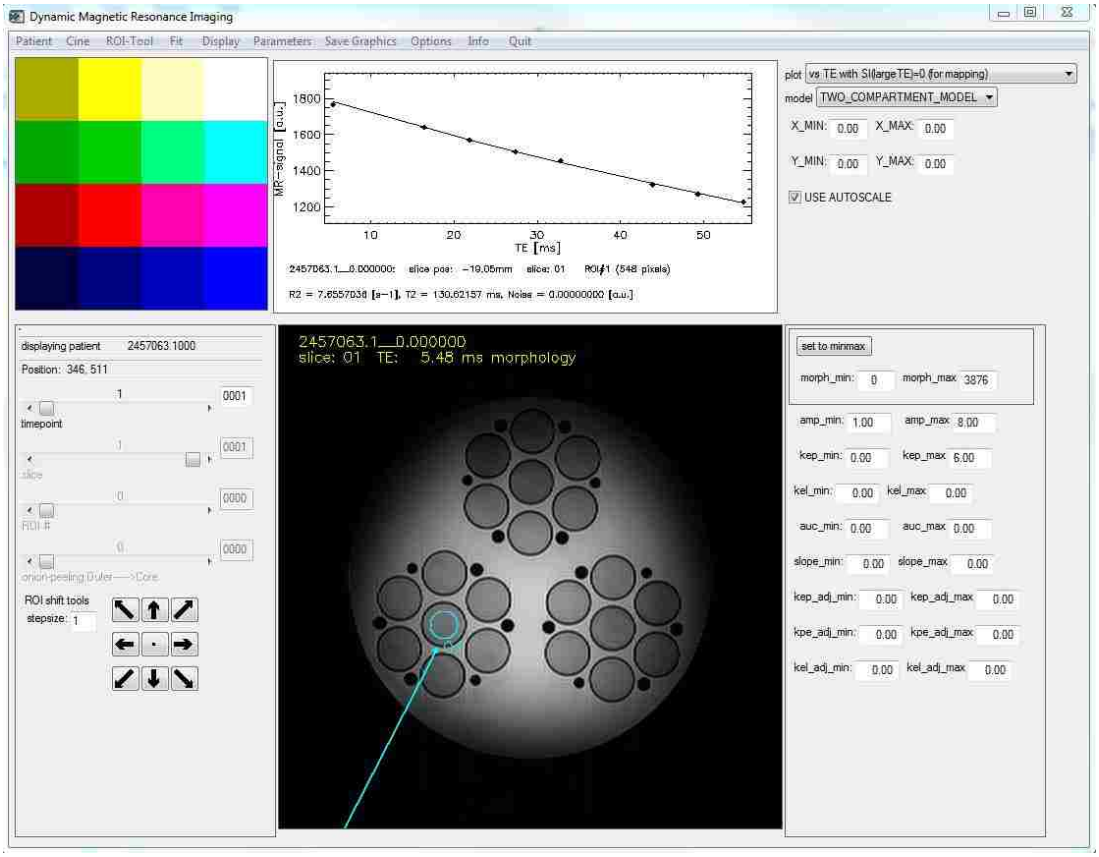

Figure 2.5: The Dynamic Magnetic Resonance Imaging Software Tool (Version OSU-5.0, Division of Imaging Research, The Ohio State University) was used to calculate T_2 values in user-defined regions of the phantom.

B_0 field inhomogeneity maps were collected after CEST-MR imaging using a 2D fast field echo (FFE) technique with the following sequence parameters: a TR of 15 ms; ΔTEs of 1

ms, 3 ms, 5 ms, 7 ms, and 9 ms; a slice thickness of 6 mm; an acquisition matrix size of 112 × 112; a field of view of 225 × 225 mm^2; NSA of 1; and a flip angle of 8˚. Reconstruction was performed automatically with the MR system software.

2.3.4 Z-SPECTRAL DATA COLLECTION

The Dynamic Magnetic Resonance Imaging Software Tool was used to extract the Z-spectral data from the CEST-MR images of the phantom. ROIs were placed in the center of each of the 21 materials with margins large enough to avoid any pixels containing the glass walls of the liquid scintillation vials. For each of the saturation amplitudes, the average signal intensity in each region collected for the 33 CEST-MR images, as well as the average signal intensity in the absence of saturation and the average B_0 field inhomogeneity.

2.3.5 Z-SPECTRAL CURVE FITTING

Prior to fitting the Z-spectral data, the frequency axis coordinates were corrected for B_0 inhomogeneity by subtracting the average B_0 value (in ppm) from the acquired frequency offsets (8 ppm to -8 ppm in 0.5 ppm increments). This corrected the lateral shift of the Z-spectra due to the B_0 field inhomogeneity.

The indices of the B_0-corrected positive and negative frequency offsets were then identified. Data points with negative frequency offsets were fit to Equation 2.2. When subsequently fitting the downfield (positive) frequency offsets, the fitted zero-frequency value from the upfield fit was included with the downfield offset data. Including this fitted upfield value in the downfield fit caused the upfield and downfield fits to meet at the 0 ppm frequency offset.

Z-spectral fitting was performed in IDL using the nonlinear least squares curve fitting package MPFIT (Markwardt 2009). Two models from literature, a 20^{th} order polynomial and a

12^{th} order polynomial, were fit to Z-spectral data for each ROI. The combination model proposed in Section 2.1 was fit with downfield polynomials of 3^{rd}, 4^{th}, 5^{th}, 6^{th}, 7^{th}, and 8^{th} orders to determine the preferred degree. Data points with signal intensities less than 5% of the signal in the absence of saturation occurred near the center of the Z-spectra, and were not included in the fitting procedure because of the poor signal-to-noise ratio of this data. For each of the 8 models applied, the AICc was calculated from the fitted Z-spectra in IDL using Equation 2.3.

2.3.6 ASSESSMENT OF MODEL PERFORMANCE

Performance of the models was assessed using the AICc values calculated after the curve fitting process. The preferred curve fitting model produced the most negative average AICc value.

2.4 AIM 2, APPLICATION OF MODEL TO PROSTATE CANCER PATIENT IMAGES

2.4.1 PROSTATE CANCER PATIENT POPULATION

Eighteen patients with biopsy-proven prostate cancer were included in this retrospective study. Thirteen of these patients underwent prostatectomy, while five received radiation therapy. An additional two volunteers were included. The average age of those enrolled in the study was 61.1 years (range, 51 to 76). Tumor staging information was available from final pathology reports for the 13 patients who underwent prostatectomy; the distribution of these tumor stages was: two T2a, one T2b, seven T2c, and three T3a. The study was approved by an institutional review board (IRB) at The Ohio State University and was compliant with the Health Insurance Portability and Accountability Act (HIPAA). Informed consent was obtained from each patient.

2.4.2 PROSTATE CANCER PATIENT IMAGING

All MR images were acquired with a 3 T MR system (Achieva, Philips Healthcare) using a 32 channel phased array coil. Images were selected based on the location of the tumor within

the prostate; CEST-MRI images were acquired using a single slice, single-shot turbo spin echo (ssTSE) pulse sequence with a TR of 4000 ms, TE of 56 ms, slice thickness of 6 mm, acquisition matrix size of 80 × 65, field of view of 140 × 140 mm^2, TSE factor of 64, NSA of 1, and flip angle of 90˚. The RF saturation pre-pulse consisted of sixteen block pulses 31 ms in duration with saturation amplitudes of 1.6 μT, 2.4 μT, 3.2 μT, and 4.0 μT. For each of the saturation amplitudes, 33 images were acquired with the saturation pre-pulse applied at offset frequencies from 8 ppm to -8 ppm in 0.5 ppm increments. An additional image was acquired without saturation as a reference. The acquisition time for this process was 3.5 minutes. Additionally, a B_0 map was obtained for each patient using a 2D fast field echo (FFE) sequence with a TR of 48 ms, TE_1 of 1.58 ms, TE_2 of 4.1 ms, slice thickness 6 mm, acquisition matrix of 80 × 65, field of view of 140 × 140 mm^2, NSA of 6, flip angle of 20˚, and acquisition time of 19.5 s. The B_0 map was created using the scanner's automatic reconstruction.

2.4.3 PROSTATE CANCER PATIENT Z-SPECTRAL DATA COLLECTION

Pathology slides were created from tissue samples from patients who underwent prostatectomy. Experienced uropathologists identified the location and extent of the tumors. The slides were digitized to create images that could be co-registered with MR images, and regions of interest (ROIs) for the peripheral zone (PZ), central gland (CG), and tumor were created by an experienced medical physicist. Patients receiving radiation therapy had ROIs delineated by the physicist based on T_2-weighted imaging and biopsy reports. An example of a pathologic slide with the marked tumor location and the resulting tumor ROI overlaid onto the CEST-MR image is shown in Figure 2.6.

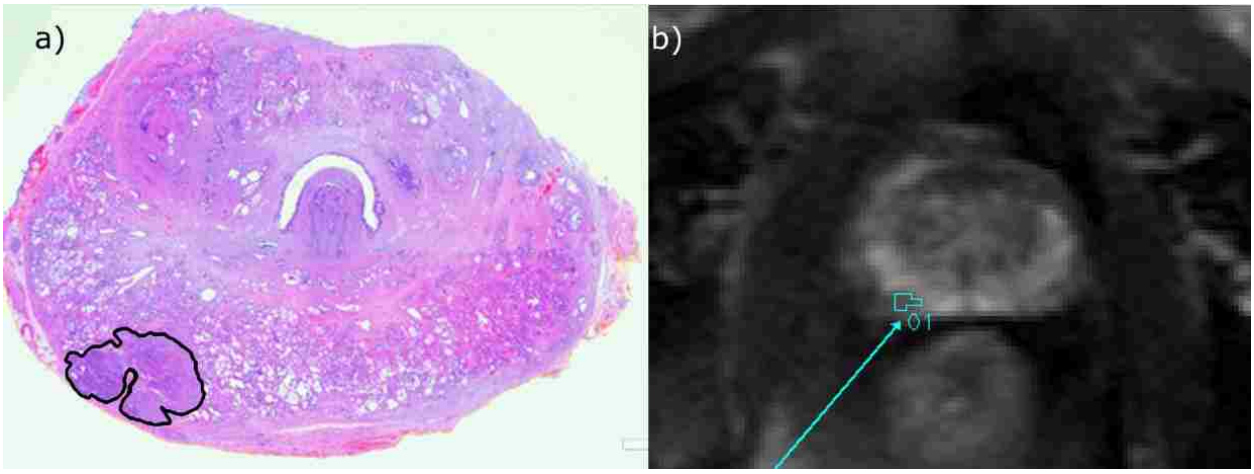

Figure 2.6: The pathologic slide created by the uropathologist (a) and the corresponding ROI drawn in the CEST-MR image (b).

Z-spectral data were extracted from the 232 resulting ROIs using the Dynamic Magnetic Resonance Imaging Software Tool. The average signal intensities for each of the 33 CEST-MR images, and the image in the absence of saturation, were recorded. The average B_0 value from the B_0 map was recorded.

2.4.4 Z-SPECTRAL CURVE FITTING

Prior to fitting the Z-spectral data, B_0 field inhomogeneity correction was performed. Z-spectral fitting was performed in as described in Section 2.3.5. The 20^{th} and 12^{th} order polynomials were used to fit the complete set of Z-spectral data. The combination models were fit with downfield polynomials of 3^{rd}, 4^{th}, 5^{th}, and 6^{th} order. These orders were selected based on the phantom results (see Section 3.1.3).

2.4.5 ASSESSMENT OF MODEL PERFORMANCE

Performance of the models was assessed using the AICc values calculated after curve fitting. The curve fitting model providing the most negative average AICc values was identified.

2.5 AIM 3, APPLICATION OF MODEL TO BLADDER CANCER PATIENT IMAGES

2.5.1 BLADDER CANCER PATIENT POPULATION

25 patients (19 male, 6 female) with biopsy-proven bladder cancer were enrolled in this study. The patients had an average age at the time of baseline imaging of 64 years (standard deviation, 12 years), and an average weight of 83.7 kg (standard deviation, 19.3 kg). The study was approved by an IRB at The Ohio State University and was HIPAA compliant. Informed consent was obtained from each patient.

2.5.2 BLADDER CANCER PATIENT IMAGING

The patients were imaged on a 3 T MR system (Achieva, Philips Healthcare) using a 32 channel cardiac surface coil. Images were acquired with a single-shot TSE sequence with the following parameters: a TR of 6100 ms; a TE of 56 ms; a TSE factor of 47; a NSA of 1; an acquisition matrix of 80 × 65; a FOV of 140 × 140 mm^2; a slice thickness of 6 mm; and a flip angle of 90˚. The acquired slice was positioned to include the tumor with the aid of T_2-weighted anatomical images. The saturation pre-pulse consisted of 16 block pulses each 29 ms in duration with a saturation amplitude of 4.0 μT; 33 CEST-MR images were acquired with the saturation pre-pulse applied at frequency offsets from 8 ppm to -8 ppm in 0.5 ppm increments. An additional image was acquired in the absence of saturation. The acquisition time for the CEST-MR images was 3.5 minutes. A B_0 field inhomogeneity map was acquired using a dual echo FFE technique with the following sequence parameters: a TR of 69.6 ms; TE of 2 ms and 10 ms; a NSA of 4; an acquisition matrix of 80 × 65; a FOV of 140 × 140 mm^2; a slice thickness of 6 mm; and a flip angle of 20˚. The acquisition time was 25 seconds. Reconstruction was performed automatically by the MR system software.

2.5.3 Z-SPECTRAL DATA COLLECTION

For each bladder cancer patient, ROIs for normal bladder wall (NBW) and tumor were delineated based on anatomical T_2-weighted images by an experienced medical physicist. The Z-spectral data in each ROI, including the average B_0 value from the field inhomogeneity map, were collected with the Dynamic Magnetic Resonance Imaging Software Tool.

2.5.4 Z-SPECTRAL CURVE FITTING

Prior to curve fitting, the B_0 inhomogeneity correction discussed in previous sections was applied. The upfield component was fit to Equation 2.1, and the downfield component was fit to a 4^{th} order polynomial, which was determined to be the preferred Z-spectral curve fitting model for phantom images with a saturation amplitude of 4.0 μT (see Section 3.2 and Section 4.4). Data points were excluded from the fitting process if the signal average at that frequency offset was less than 5% of the signal intensity in the absence of saturation, to avoid data points with a low signal-to-noise ratio.

2.5.5 DISTINGUISHING NORMAL BLADDER WALL FROM CANCER

The shifted, fitted Z-spectra were used to calculate MTR_{asym} at frequency offsets of 2.0 ppm and 3.5 ppm, corresponding to the amine and amide protons, respectively. A two-tailed, paired Student's *t*-test was used to test for significant differences in the MTR_{asym}(2.0 ppm) and MTR_{asym}(3.5 ppm) quantities between the NBW and tumor regions. A Shapiro-Wilk test was performed to confirm that the data was normally distributed. These tests were performed using the statistical analysis software, R (Version 3.1.0, R Development Core Team). *P*-values less than 0.05 were considered significant for all tests.

CHAPTER 3: RESULTS

3.1 RESULTS FOR AIM 1: PHANTOM MODEL SELECTION

3.1.1 PHANTOM PROPERTIES

Average values for T_1 and T_2 relaxation times and the associated standard deviations and standard errors are contained in Table 3.1. Standard deviations for T_1 are the standard deviation of pixel values from the T_1 map, while standard errors for T_2 measurements are from the Dynamic Magnetic Resonance Imaging Software Tool.

Table 3.1: Average T_1 and T_2 relaxation times and the associated standard deviations (σ_{T1}) or standard errors (SE_{T2}) for the regions of the phantom. Table 2.1 contains the concentration values for A, B, and C.

Material	Concentration	T_1 (ms)	σ_{T1} (ms)	T_2 (ms)	SE_{T2} (ms)
Agar	A	2360	170	136	6
	B	1910	540	66	2
	C	1710	120	56	2
Choline	A	2370	140	125	7
	B	2410	150	136	6
	C	2410	170	145	6
Creatine	A	2500	300	190	13
	B	2340	160	153	6
	C	2550	430	167	17
Glucose	A	2410	150	146	6
	B	2320	120	115	5
	C	2350	150	112	4
Glycogen	A	2410	120	131	8
	B	2240	110	121	5
	C	2060	390	114	4
Lysine	A	2400	310	129	2
	B	2370	260	115	7
	C	2480	660	154	27
NH_4Cl	A	2480	210	130	6
	B	2630	420	101	6
	C	2660	605	99	8
Water		2960	180	1030	520

The B_0 field inhomogeneity maps are shown in Figure 3.1. The measured B_0 field inhomogeneity increased with increasing difference in echo times. The B_0 field inhomogeneity

map with a ΔTE of 5 ms was used for the CEST-MR image post processing because it was the largest echo time difference that did not produce noticeable artifacts due to large phase differences.

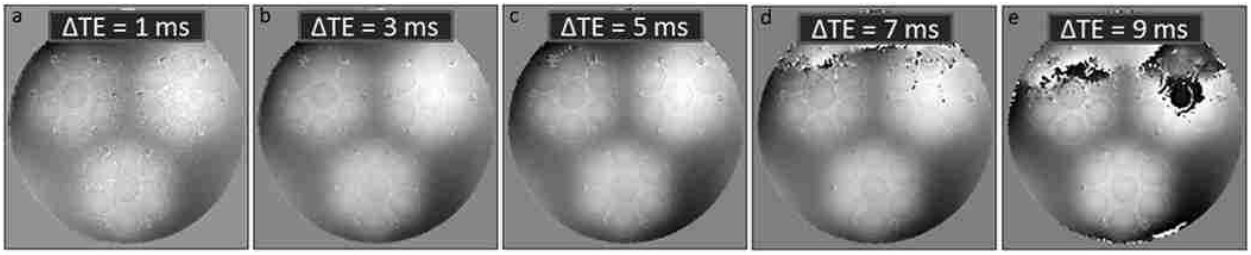

Figure 3.1: The B_0 field inhomogeneity maps created with echo time differences of (a) 1 ms, (b) 3 ms, (c) 5 ms, (d) 7 ms, and (e) 9 ms. A phase wrapping artifact is evident for echo time differences of 7 ms and 9 ms.

3.1.2 PHANTOM CURVE FITTING RESULTS

Representative examples of the curve fitting results for CEST-MR Z-spectra with a saturation amplitude of 1.6 μT are shown in Figure 3.2. The Z-spectra from a low saturation amplitude were more sharply peaked than those from higher saturation amplitudes. This caused the combination models using low order polynomials to perform poorly visually in the region of the Z-spectrum upfield from water resonance, indicated by the arrow in Figure 3.2a. The combination models using higher order polynomials perform well visually, though the 8^{th} order combination model shows some oscillation near the end of the fitting interval, indicated by the arrow in Figure 3.2b. The two polynomial models both experience significant oscillation near the ends of the fitting intervals, indicated by the arrows in Figure 3.2c and Figure 3.2d.

Representative examples of the curve fitting results for CEST-MR Z-spectra with a saturation amplitude of 4.0 μT are shown in Figure 3.3. At this high saturation amplitude, the Z-spectra became less sharply peaked. The broader shape of the Z-spectra decreased the size of the oscillations near the edges of the interval for all models, and in many cases eliminated all oscillations. The visual performance of the combination model using a low order polynomial

improved as the saturation amplitude increased, as shown by the difference between Figure 3.2a and Figure 3.3a. In some cases, the combination models using high order polynomials had large deviations from the expected shape due to the excluded data points around 0 ppm, indicated by the arrow in Figure 3.3b. The 12th order polynomial performed well visually at this high saturation amplitude, shown in Figure 3.3c. The 20th order polynomial exhibited oscillations even at this high saturation amplitude, shown in Figure 3.3d.

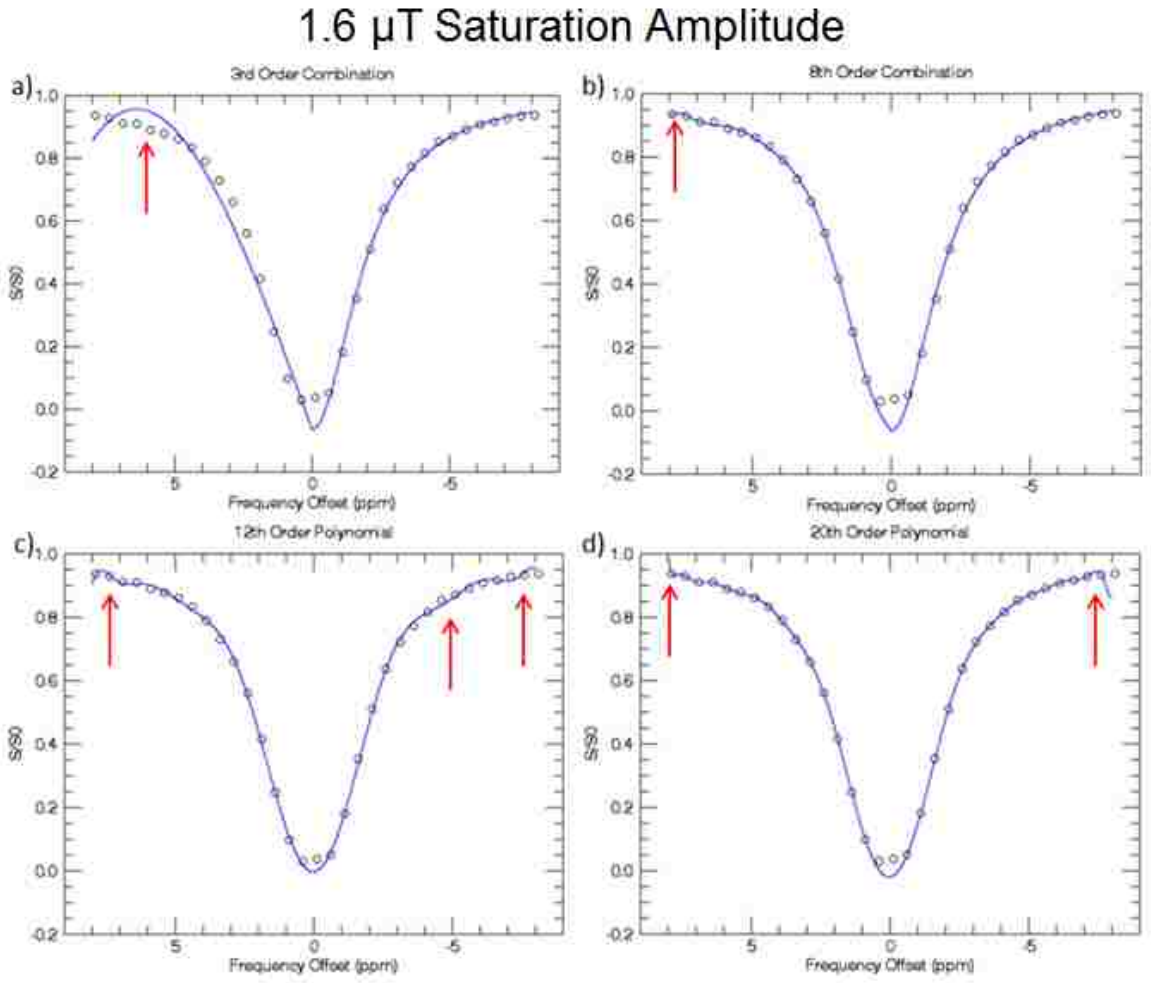

Figure 3.2: The Z-spectrum for Glucose concentration C with a saturation amplitude of 1.6 µT fit with (a) the 3rd order combination model, (b) the 8th order combination model, (c) the 12th order polynomial model, and (d) the 20th order polynomial model.

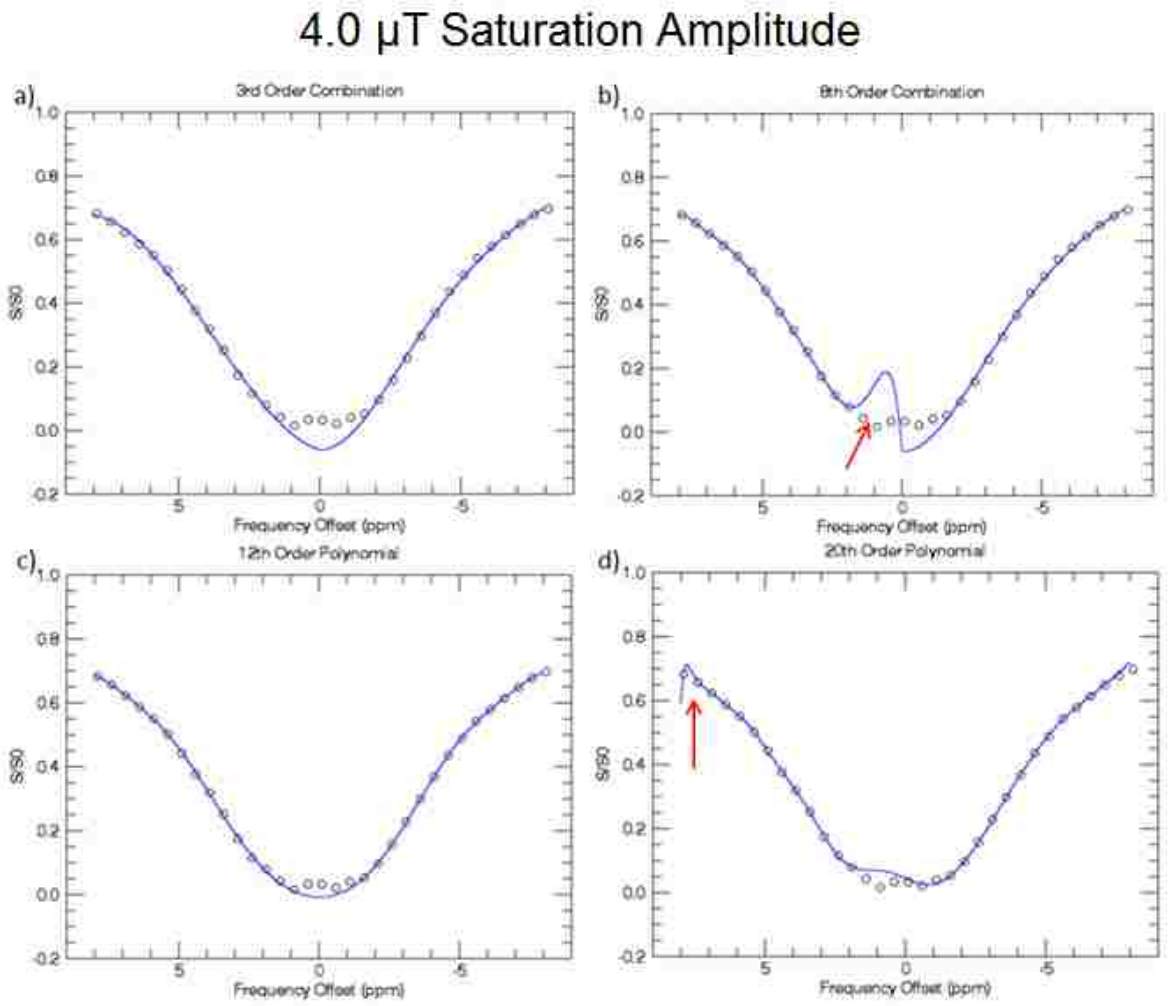

Figure 3.3: The Z-spectrum for Glucose concentration C with a saturation amplitude of 4.0 µT fit with (a) the 3rd order combination model, (b) the 8th order combination model, (c) the 12th order polynomial model, and (d) the 20th order polynomial model.

3.1.3 PHANTOM MODEL SELECTION

The distributions of AICc values for the Z-spectra with a saturation amplitude of 1.6 µT are displayed as boxplots in Figure 3.4. The average AICc values are listed in Table 3.2, ordered by increasing average AICc. The combination models utilizing low order polynomials did not perform well at this saturation amplitude using the AICc as a metric due to a high residual sum of squares. The large AICc of the high order polynomial fitting was due to the large number of fitting parameters rather than the goodness of fit. The 6th order combination was the preferred

model for the 1.6 μT saturation amplitude as it has the most negative maximum AICc of the subset of models with the most negative but statistically indistinguishable average AICc.

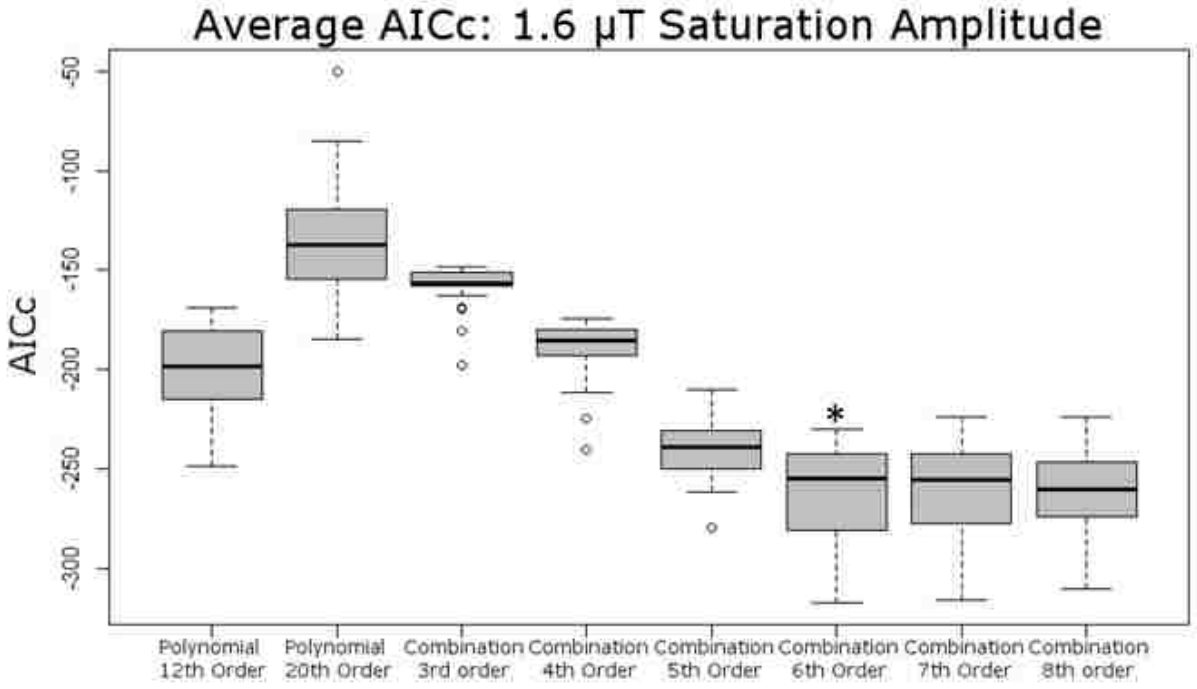

Figure 3.4: The distributions of AICc values averaged over all material concentrations with the saturation amplitude of 1.6 μT. The averages indicated on the boxplots are median values. * indicates the preferred model.

Table 3.2: AICc results of the models for the saturation amplitude of 1.6 μT, ordered by increasing average AICc.

Rank	Model	$AICc_{mean}$	σ_{AICc}	$AICc_{min}$	$AICc_{max}$
1	Combination, 6th order	-263.0	24.3	-317.4	-229.9
2	Combination, 7th order	-261.5	24.6	-316.2	-224.0
3	Combination, 8th order	-261.4	23.7	-310.8	-223.9
4*	Combination, 5th order	-240.9	17.1	-279.6	-210.1
5**	Polynomial, 12th order	-200.7	23.5	-248.4	-169.1
6**	Combination, 4th order	-190.8	16.6	-240.1	-174.1
7**	Combination, 3rd order	-158.7	12.0	-197.7	-148.5
8**	Polynomial, 20th order	-133.9	32.2	-184.9	-49.9

* indicates a significant difference ($p < 0.05$) between the marked model and the model with the minimum AICc. ** indicates $p < 0.001$.

The distributions of AICc values for the Z-spectra with a saturation amplitude of 2.4 μT are displayed as boxplots in Figure 3.5. The average AICc values for each model and the associated standard deviations, minimums, and maximums are listed in Table 3.3. The 4th and 5th

order combination models showed lower average AICc compared to the 1.6 μT saturation amplitude Z-spectra, with the 5th order combination having the most negative average AICc. As with the 1.6 μT saturation amplitude, the poor performance of the 20th order polynomial model was due to the large number of fitting parameters relative to the number of data points, while the poor performance of the 3rd order combination model was due to the relatively high sum of squared residuals. The 5th order polynomial model was the preferred model for the 2.4 μT saturation amplitude because it had the most negative maximum AICc of the subset of models with the most negative but statistically indistinguishable average AICc.

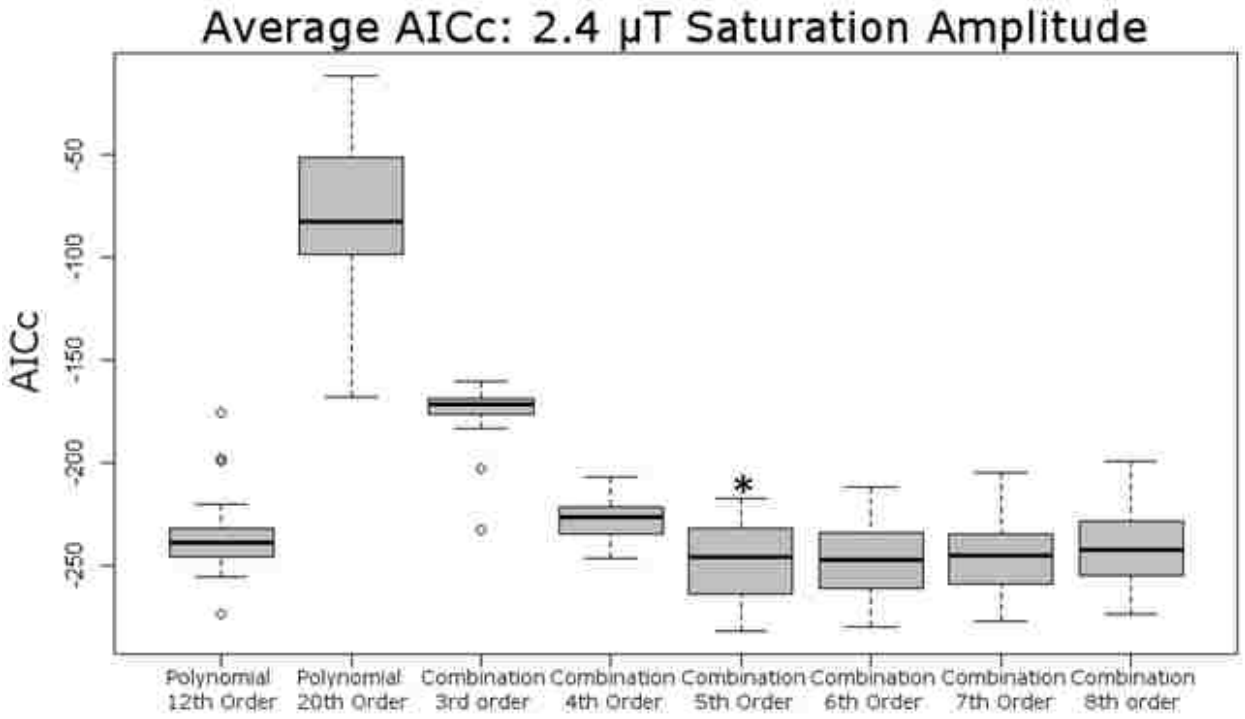

Figure 3.5: The distributions of AICc values averaged over all material concentrations with the saturation amplitude of 2.4 μT. The averages indicated on the boxplots are median values. * indicates the preferred model.

The distributions of AICc values for Z-spectra with a saturation amplitude of 3.2 μT are displayed as boxplots in Figure 3.6. The average AICc values for each model are listed in Table 3.4. The relatively large saturation amplitude improved the performance of the combination

model relying on the lower order polynomials to fit the region of the Z-spectra upfield from water resonance. The average AICc values for the 20th order polynomial continued to increase as more data points fell below the exclusion threshold for the fitting procedure which further increased the ratio of fitting parameters to the number of data points. The 6th order combination model was the preferred model for the 3.2 μT saturation amplitude because it had the most negative maximum AICc of the subset of models with the most negative but statistically indistinguishable average AICc.

Table 3.3: AICc results of the models for the saturation amplitude of 2.4 μT, ordered by increasing average AICc.

Rank	Model	$AICc_{mean}$	σ_{AICc}	$AICc_{min}$	$AICc_{max}$
1	Combination, 5th order	-248.3	20.1	-282.1	-217.8
2	Combination, 6th order	-246.2	20.4	-279.8	-212.1
3	Combination, 7th order	-245.8	20.1	-277.5	-205.2
4*	Combination, 8th order	-241.3	20.9	-273.6	-199.7
5**	Polynomial, 12th order	-235.0	21.5	-273.9	-176.1
6**	Combination, 4th order	-227.5	10.5	-246.5	-206.9
7**	Combination, 3rd order	-175.3	16.0	-232.9	-160.9
8**	Polynomial, 20th order	-79.2	34.9	-168.4	-12.0

* indicates a significant difference ($p < 0.05$) between the marked model and the model with the minimum AICc. ** indicates $p < 0.001$.

The distributions of AICc values for the Z-spectra with a saturation amplitude of 4.0 μT are displayed as boxplots in Figure 3.7. The average AICc values for each model are listed in Table 3.5. The performance of the combination models using low order polynomials improved further at the large saturation amplitude, with the 5th order combination model having the most negative average AICc value and the 4th order combination having the most negative maximum AICc value. The AICc values for the 20th order polynomial continued to increase with increasing saturation amplitude as more data points fell below the exclusion threshold and the ratio of fitting parameters to data points increased further. The 4th order combination was the preferred

model because there was no significant difference ($p > 0.05$) between the average AICc value for the 4th order combination and 6th order combination models, but the 4th order combination model had the most negative maximum AICc value.

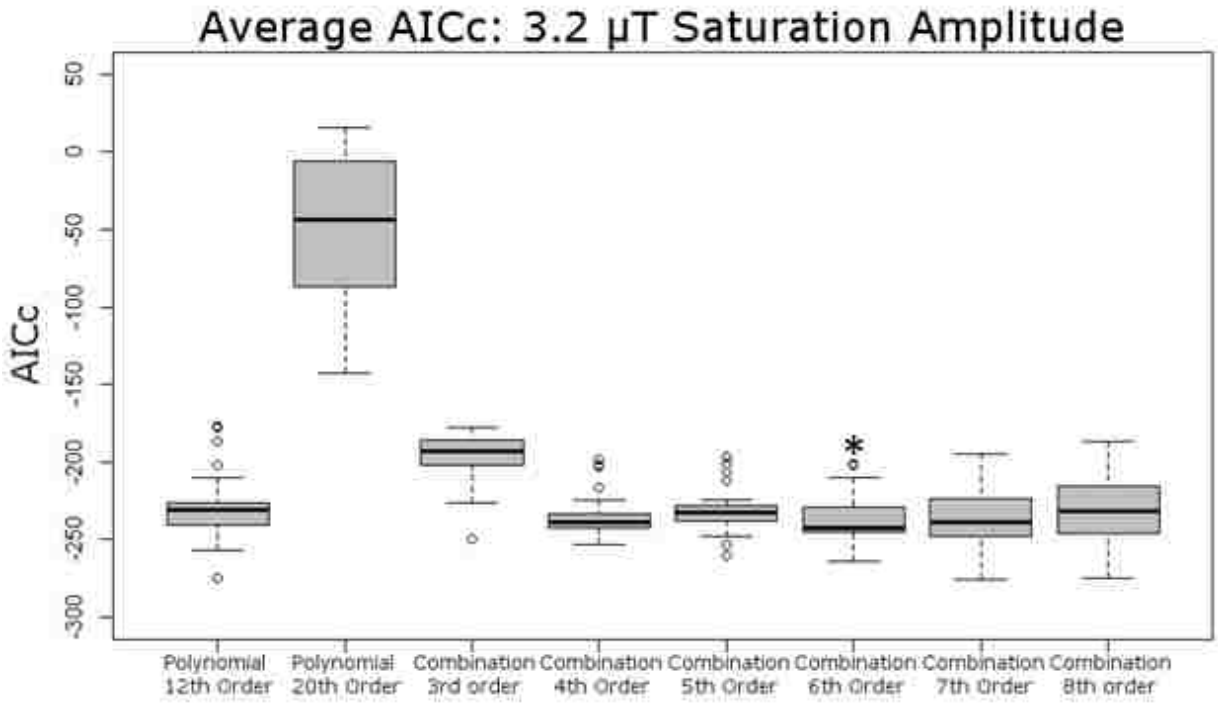

Figure 3.6: The distributions of AICc values averaged over all material concentrations with the saturation amplitude of 3.2 μT. The averages indicated on the boxplots are median values. * indicates the preferred model.

Table 3.4: AICc results of the models for the saturation amplitude of 3.2 μT, ordered by increasing average AICc.

Rank	Model	$AICc_{mean}$	σ_{AICc}	$AICc_{min}$	$AICc_{max}$
1	Combination, 6th order	-237.3	17.1	-264.3	-200.7
2	Combination, 7th order	-236.4	21.0	-275.4	-194.8
3	Combination, 4th order	-233.9	16.1	-253.5	-198.5
4	Combination, 5th order	-230.6	15.9	-260.8	-196.4
5	Combination, 8th order	-230.6	22.3	-275.3	-186.9
6	Polynomial, 20th order	-227.5	24.7	-274.7	-176.4
7**	Combination, 3rd order	-197.0	16.7	-249.5	-178.1
8**	Polynomial, 20th order	-41.9	68.1	-143.0	186.3

* indicates a significant difference ($p < 0.05$) between the marked model and the model with the minimum AICc. ** indicates $p < 0.001$.

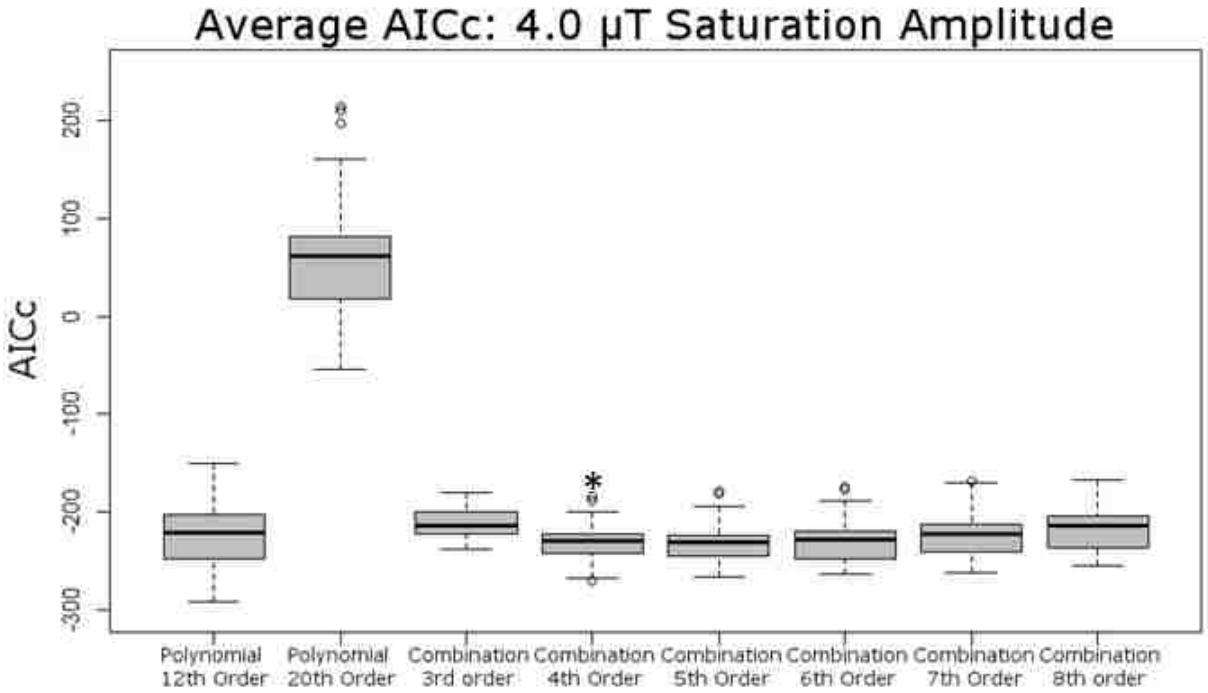

Figure 3.7: The distributions of AICc values averaged over all material concentrations with the saturation amplitude of 4.0 μT. The averages indicated on the boxplots are median values. * indicates the preferred model.

Table 3.5: AICc results of the models for the saturation amplitude of 4.0 μT, ordered by increasing average AICc.

Rank	Model	$AICc_{mean}$	σ_{AICc}	$AICc_{min}$	$AICc_{max}$
1	Combination, 5th order	-229.9	23.6	-266.5	-178.7
2	Combination, 4th order	-229.3	22.4	-270.3	-184.3
3	Combination, 6th order	-228.1	25.3	-263.4	-173.7
4	Combination, 7th order	-222.3	26.0	-262.1	-168.3
5	Polynomial, 12th order	-221.2	35.9	-291.2	-149.5
6	Combination, 8th order	-215.9	25.2	-254.3	-167.0
7**	Combination, 3rd order	-211.5	16.1	-238.2	-179.5
8**	Polynomial, 20th order	105.1	201.3	-53.7	920.3

* indicates a significant difference ($p < 0.05$) between the marked model and the model with the minimum AICc. ** indicates $p < 0.001$.

The distributions of AICc values for the combination of all saturation amplitudes are displayed as boxplots in Figure 3.8. The average AICc values for the combination of all saturation amplitudes are listed in Table 3.6. Although the model with the most negative AICc value was the 6th order combination, there was no significant difference ($p > 0.05$) between AICc values for the 5th, 6th, 7th, and 8th order combination models. Because of this, the 5th order

combination was identified as the preferred model because it had the most negative maximum AICc value of that group of models.

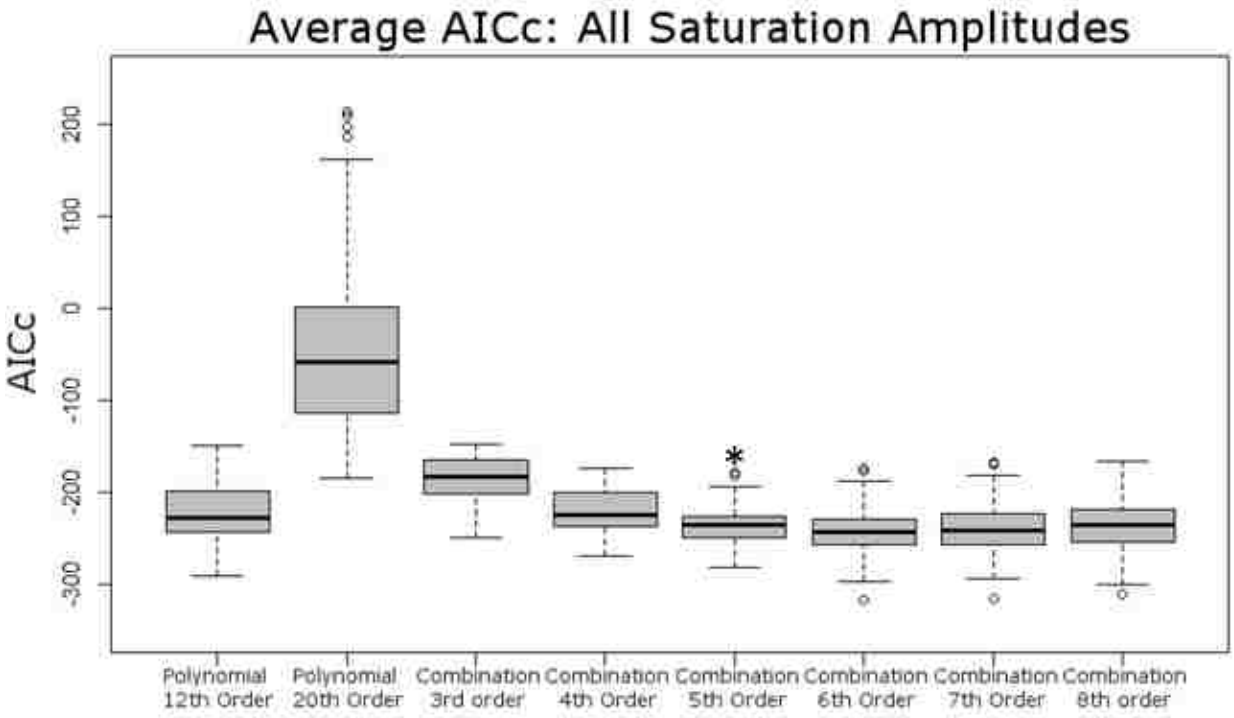

Figure 3.8: The distributions of AICc values for all of the fitting models tested for the CEST-MRI phantom at all saturation amplitudes. * indicates the preferred model.

Table 3.6: AICc results of the models for all saturation amplitudes, ordered by increasing average AICc.

Rank	Model	$AICc_{mean}$	σ_{AICc}	$AICc_{min}$	$AICc_{max}$
1	Combination, 6^{th} order	-243.7	25.2	-317.4	-173.7
2	Combination, 7^{th} order	-241.5	26.8	-316.2	-168.3
3	Combination, 5^{th} order	-237.4	20.5	-282.1	-178.7
4	Combination, 8^{th} order	-237.3	28.1	-310.8	-167.0
5*	Polynomial, 12^{th} order	-221.1	29.4	-291.2	-149.5
6*	Combination, 4^{th} order	-220.4	24.1	-270.3	-174.1
7**	Combination, 3^{rd} order	-185.6	25.3	-249.5	-148.5
8**	Polynomial, 20^{th} order	-37.5	139.2	-184.9	920.3

* indicates a significant difference ($p < 0.05$) between the marked model and the model with the minimum AICc. ** indicates $p < 0.001$.

The preferred model selected by the AICc depended on the amplitude of the saturation pre-pulse. Table 3.7 lists the preferred fitting model for each of the saturation amplitudes tested. A combination models was preferred for all saturation amplitudes tested, and the order of the polynomial used for the portion of the Z-spectrum upfield from water resonance decreased with increasing saturation amplitude.

Table 3.7: The preferred fitting models for the CEST-MRI phantom images as selected by AICc for each of the saturation amplitudes tested.

Saturation Amplitude	Preferred Model
1.6 μT	6^{th} Order Combination
2.4 μT	5^{th} Order Combination
3.2 μT	6^{th} Order Combination
4.0 μT	4^{th} Order Combination
All Amplitudes	5^{th} Order Combination

3.2 RESULTS FOR AIM 2: MODEL SELECTION WITH PATIENT IMAGES

3.2.1 PROSTATE CANCER PATIENT CURVE FITTING RESULTS

A representative sample of the curve fitting results for Z-spectra acquired from the prostate cancer patient images with a saturation amplitude of 1.6 μT is plotted in Figure 3.9, with deviations from the data indicated with arrows. As with Z-spectra from phantom images, those acquired with low saturation amplitudes were more sharply peaked and experienced significant oscillation near the edge of the fitting interval. The low order combination models did not perform well when the Z-spectra were sharply peaked, and all of the models experienced at least some deviations.

A representative sample of the curve fitting results for a Z-spectrum acquired from the prostate cancer patient images with the saturation amplitude of 4.0 μT is plotted in Figure 3.10. The increased saturation amplitude increased the width of the DWS contribution. The 3^{rd} order combination model appeared to have inadequacies at this saturation amplitude, indicated by the

arrow in Figure 3.10a, while the higher order combination models, shown in Figure 3.10b, performed well visually. Oscillations near the edge of the interval were greatly reduced for the 12th order polynomial model, shown in Figure 3.10c. The 20th order polynomial, shown in Figure 3.10d, exhibited oscillations near the edge of the interval for this saturation amplitude.

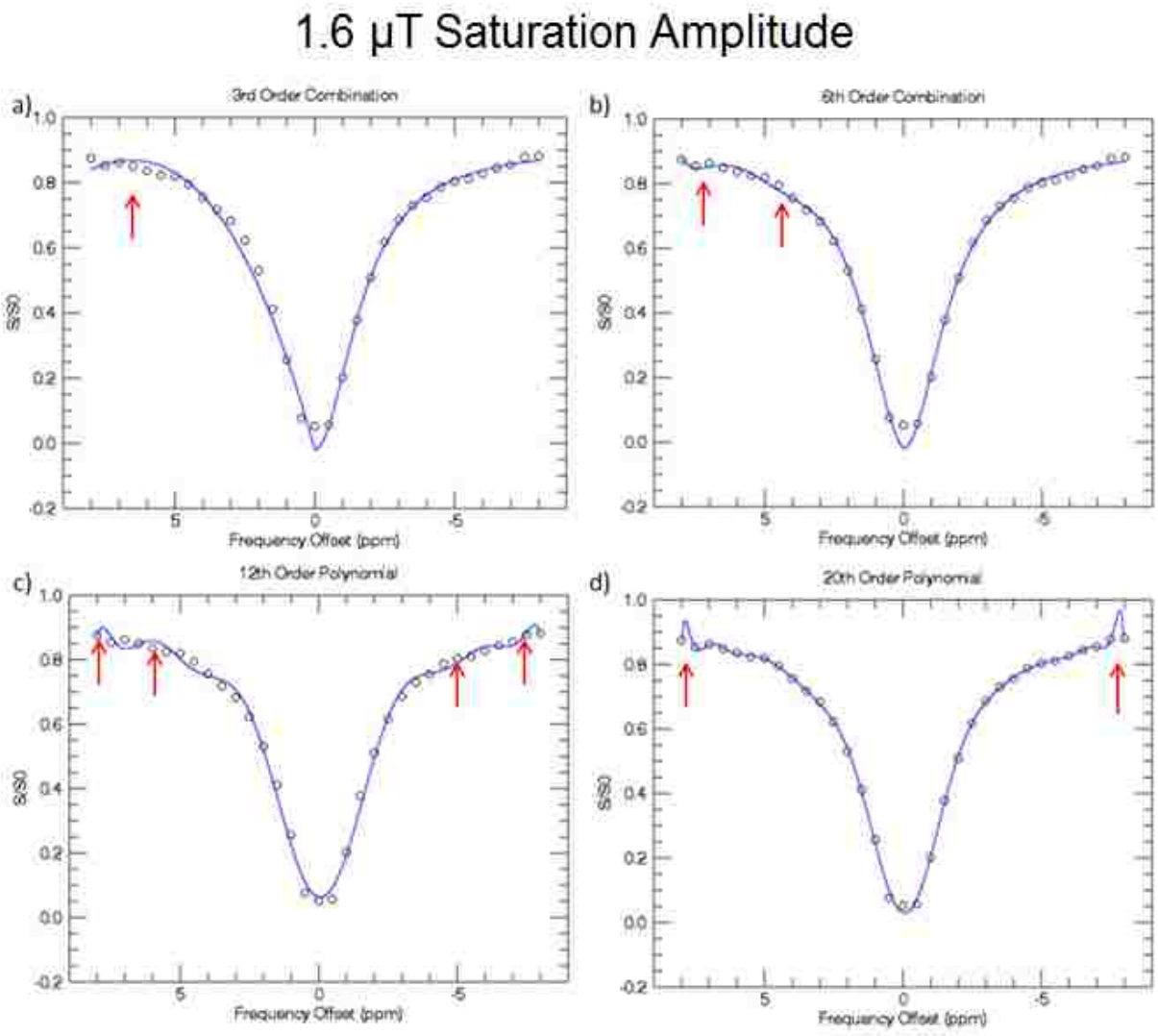

Figure 3.9: The Z-spectrum of the central gland region of the prostate from an image set acquired with a saturation amplitude of 1.6 µT. The Z-spectrum was fit with (a) the 3rd order combination model, (b) the 6th order combination model, (c) the 12th order polynomial model, and (d) the 20th order polynomial model.

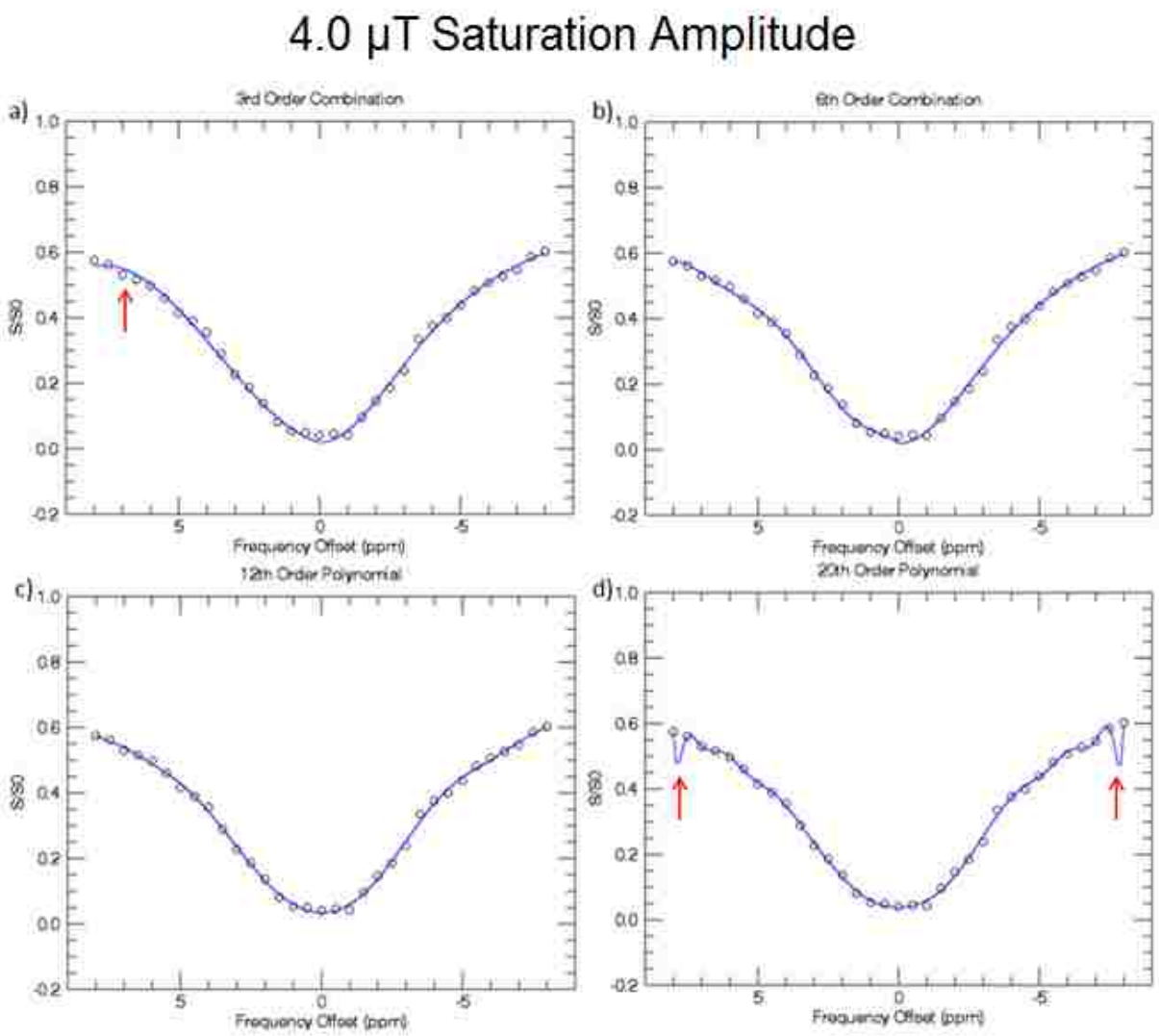

Figure 3.10: The Z-spectrum of the central gland region of the prostate from an image set acquired with a saturation amplitude of 4.0 µT. The Z-spectrum was fit with (a) the 3rd order combination model, (b) the 6th order combination model, (c) the 12th order polynomial model, and (d) the 20th order polynomial model.

3.2.2 PATIENT MODEL SELECTION

The distributions of AICc values for the Z-spectra with a saturation amplitude of 1.6 µT are displayed as boxplots in Figure 3.11. The average AICc for each model is listed in Table 3.8, ordered by increasing average AICc. The combination models outperformed the high order polynomial models using the AICc as a metric due to the polynomials' high ratio of fitting

parameters to the number of data points, though this is not visually apparent in Figure 3.9. The 5th and 6th order combination models outperformed the 3rd and 4th order combination models due to their smaller residual sums of squares. The 6th order combination was the preferred model for the 1.6 μT saturation amplitude because it had the most negative average AICc.

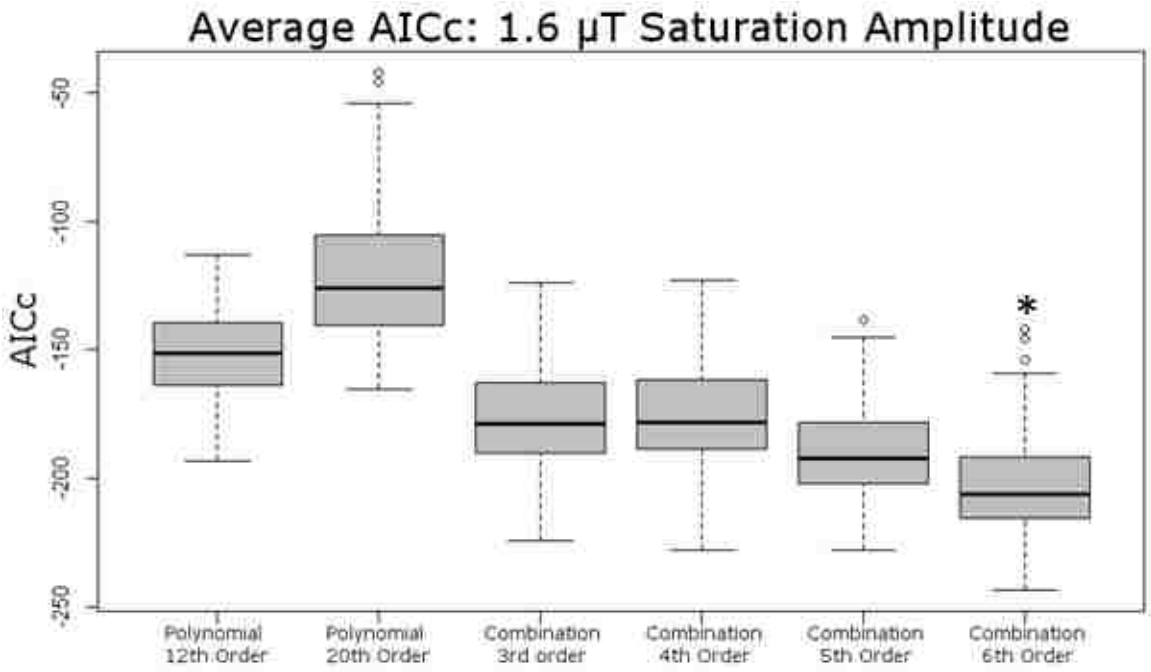

Figure 3.11: The distributions of AICc values for all regions of the prostate with a saturation amplitude of 1.6 μT. The averages indicated on the boxplots are median values.* indicates the preferred model.

Table 3.8: AICc results of the models for the saturation amplitude of 1.6 μT for the prostate cancer patient images.

Rank	Model	$AICc_{mean}$	σ_{AICc}	$AICc_{min}$	$AICc_{max}$
1	Combination, 6th order	-200.9	23.2	-243.3	-141.8
2*	Combination, 5th order	-189.6	20.4	-227.6	-138.2
3**	Combination, 4th order	-177.3	20.5	-228.0	-123.1
4**	Combination, 3rd order	-176.5	21.8	-224.2	-124.2
5**	Polynomial, 12th order	-151.7	17.7	-193.1	-113.2
6**	Polynomial, 20th order	-120.7	30.9	-165.2	-42.2

* indicates a significant difference ($p < 0.05$) between the marked model and the model with the minimum AICc. ** indicates $p < 0.001$.

The distributions of AICc values for the Z-spectra with a saturation amplitude of 2.4 μT are displayed as boxplots in Figure 3.12. The average AICc for each model is listed in Table 3.9, ordered by increasing average AICc. The combination models outperformed the 20th order polynomial model, though the 12th order polynomial model outperformed both the 3rd and 4th order combination models. The 5th order combination was the preferred model for a 2.4 μT saturation amplitude because it had the smallest maximum AICc of the subset of models with the most negative but statistically indistinguishable average AICc.

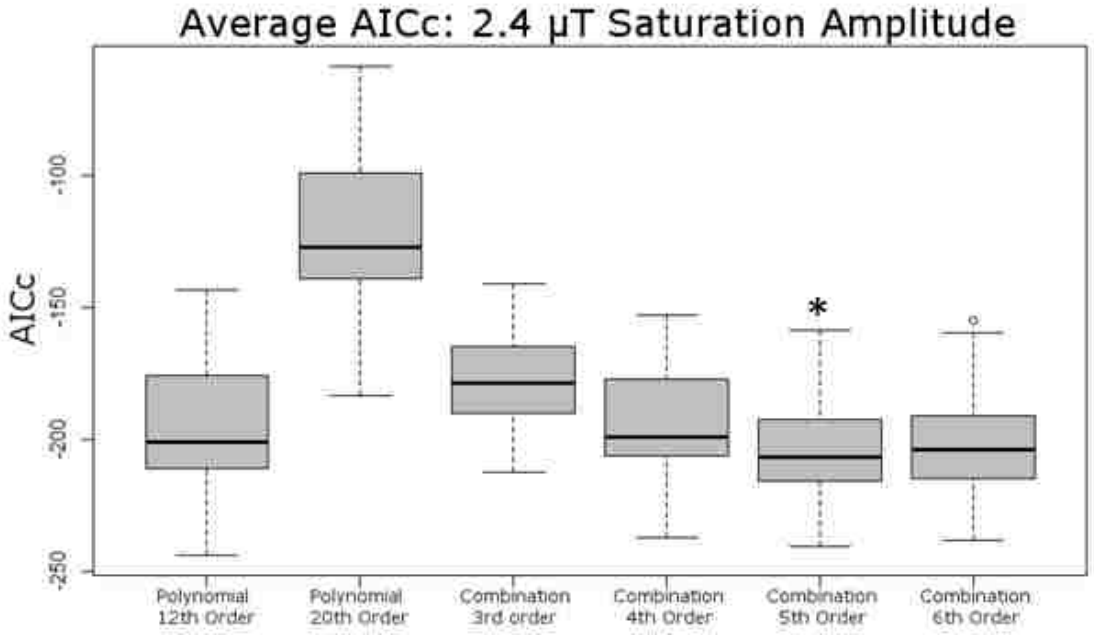

Figure 3.12: The distributions of AICc values for all regions of the prostate with a saturation amplitude of 2.4 μT. The averages indicated on the boxplots are median values. * indicates the preferred model.

The distributions of AICc values for the Z-spectra with a saturation amplitude of 3.2 μT are displayed as boxplots in Figure 3.13. The average AICc values for the saturation amplitude of 3.2 μT are listed in Table 3.10, ordered by increasing average AICc. As saturation amplitude increased, the Z-spectra broadened, and the performances of the low order polynomials within the combination models improved, as seen in Figure 3.10. The visual performance improvement

at higher saturation amplitudes seen for the 12th order polynomial model was reflected in the AICc values. The 4th order combination was identified as the preferred model because it had the most negative maximum AICc value of the subset of models with the most negative but statistically indistinguishable average AICc.

Table 3.9: AICc results of the models for the saturation amplitude of 2.4 μT for the prostate cancer patient images.

Rank	Model	$AICc_{mean}$	σ_{AICc}	$AICc_{min}$	$AICc_{max}$
1	Combination, 5th order	-202.6	20.5	-240.3	-158.6
2	Combination, 6th order	-200.3	19.6	-237.9	-154.7
3	Polynomial, 12th order	-195.1	24.7	-243.7	-143.4
4*	Combination, 4th order	-193.6	19.4	-236.9	-153.0
5**	Combination, 3rd order	-177.2	15.4	-212.5	-141.3
6**	Polynomial, 20th order	-122.7	27.5	-183.2	-58.7

* indicates a significant difference ($p < 0.05$) between the marked model and the model with the minimum AICc. ** indicates $p < 0.001$.

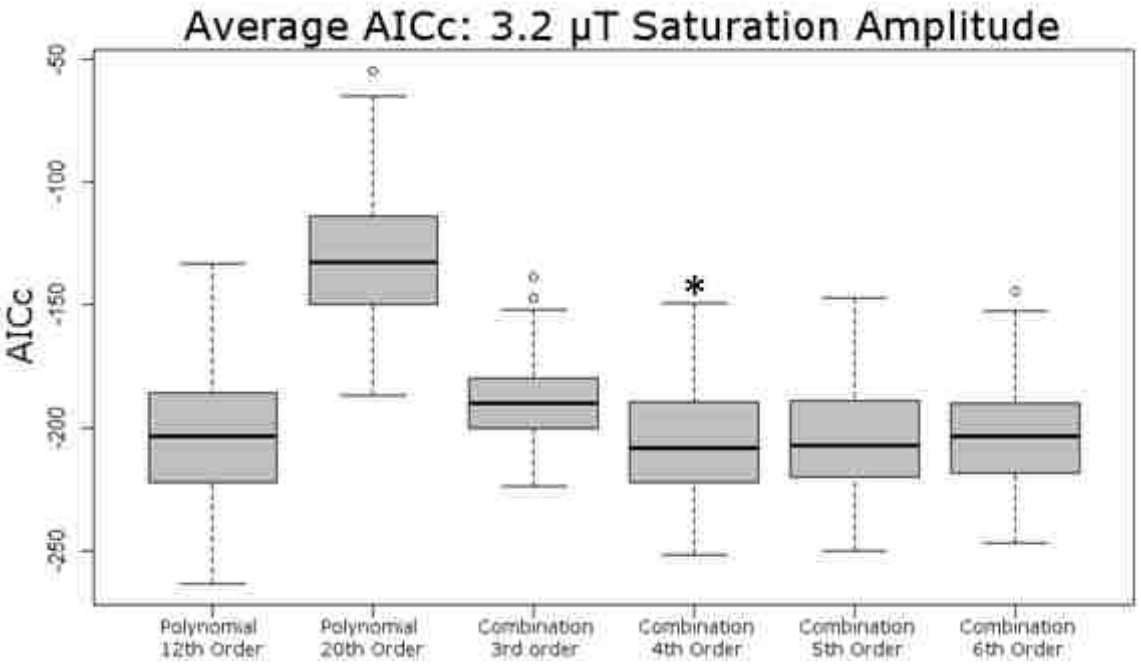

Figure 3.13: The distributions of AICc values for all regions of the prostate with a saturation amplitude of 3.2 μT. The averages indicated on the boxplots are median values. * indicates the preferred model.

Table 3.10: AICc results of the models for the saturation amplitude of 3.2 μT for the prostate cancer patient images.

Rank	Model	$AICc_{mean}$	σ_{AICc}	$AICc_{min}$	$AICc_{max}$
1	Combination, 4th order	-204.9	24.1	-251.6	-149.1
2	Combination, 5th order	-203.8	23.7	-250.2	-147.2
3	Combination, 6th order	-200.8	23.4	-246.9	-144.5
4	Polynomial, 12th order	-200.7	27.3	-263.4	-133.1
5**	Combination, 3rd order	-188.6	18.2	-223.8	-138.3
6**	Polynomial, 20th order	-129.5	30.7	-186.9	-54.8

* indicates a significant difference ($p < 0.05$) between the marked model and the model with the minimum AICc. ** indicates $p < 0.001$.

The distributions of AICc values for the Z-spectra with a saturation amplitude of 4.0 μT are displayed as boxplots in Figure 3.11. The average AICc values are listed in Table 3.12. Though there were no statistically significant differences in average AICc value between the 3rd, 4th, 5th, or 6th combination models or 12th order polynomial model, the 3rd order combination model was preferred because it has the most negative maximum AICc.

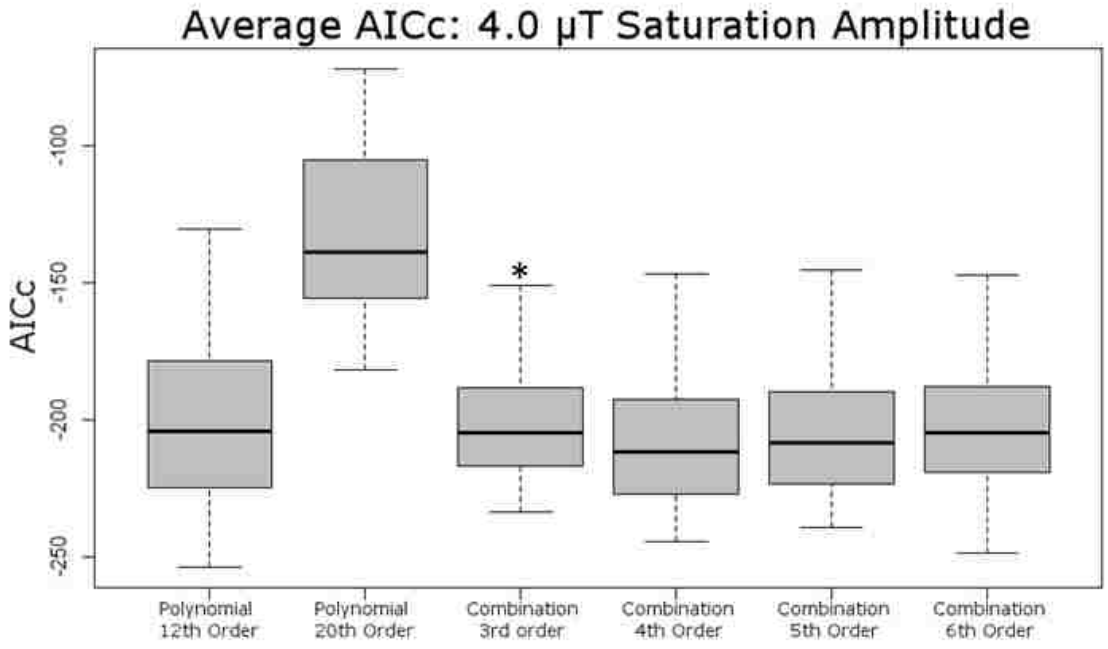

Figure 3.14: The distributions of AICc values for all regions of the prostate with a saturation amplitude of 4.0 μT. The averages indicated on the boxplots are median values. * indicates the preferred model.

The distributions of AICc values for the Z-spectra at all saturation amplitudes are displayed as boxplots in Figure 3.15, and the average AICc values for all saturation amplitudes are listed in Table 3.12. There was no significant difference in average AICc values between the 5th and 6th order combination models. The preferred model considering all saturation amplitudes was the 6th order combination model, which had the smallest maximum AICc between the subset of models with the most negative but statistically indistinguishable average AICc.

Table 3.11: AICc results of the models for the saturation amplitude of 4.0 μT for the prostate cancer patient images.

Rank	Model	$AICc_{mean}$	σ_{AICc}	$AICc_{min}$	$AICc_{max}$
1	Combination, 4th order	-208.9	23.1	-244.2	-146.9
2	Combination, 5th order	-205.0	23.1	-239.1	-145.4
3	Combination, 6th order	-203.0	22.8	-248.4	-147.3
4	Combination, 3rd order	-201.6	20.6	-233.5	-150.9
5	Polynomial, 12th order	-200.1	27.5	-253.7	-130.3
6**	Polynomial, 20th order	-132.1	30.1	-181.7	-71.9

* indicates a significant difference ($p < 0.05$) between the marked model and the model with the minimum AICc. ** indicates $p < 0.001$.

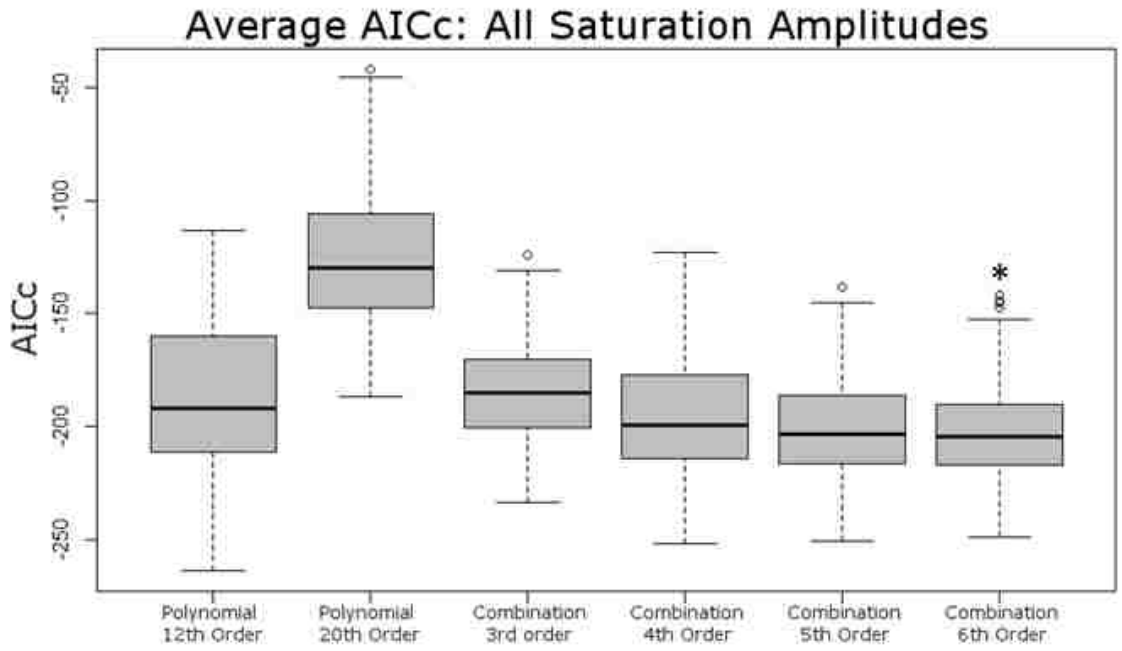

Figure 3.15: The distributions of AICc values for all regions of the prostate and all saturation amplitudes. The averages indicated on the boxplots are median values. * indicates the preferred model.

Table 3.12: AICc results of the models for all saturation amplitudes for the prostate cancer patient images.

Rank	Model	$AICc_{mean}$	σ_{AICc}	$AICc_{min}$	$AICc_{max}$
1	Combination, 6^{th} order	-201.3	22.2	-248.4	-141.8
2	Combination, 5^{th} order	-200.2	22.7	-250.2	-138.2
3*	Combination, 4^{th} order	-196.2	24.9	-251.6	-123.1
4**	Polynomial, 12^{th} order	-186.9	31.9	-263.4	-113.2
5**	Combination, 3^{rd} order	-186.0	21.6	-233.5	-124.2
6**	Polynomial, 20^{th} order	-126.2	30.0	-186.9	-42.2

* indicates a significant difference ($p < 0.05$) between the marked model and the model with the minimum AICc. ** indicates $p < 0.001$.

The preferred model selected by the AICc depended on the saturation amplitude. Table 3.13 lists the preferred fitting model for each of the saturation amplitudes tested. As seen with the phantom images, the combination models were preferred to the high order polynomial models for all saturation amplitudes tested, and increasing saturation amplitude decreased the required order of the polynomial used for the portion of the Z-spectrum upfield from water resonance.

Table 3.13: The preferred fitting models for the prostate cancer patient images as selected by AICc for each of the saturation amplitudes tested.

Saturation Amplitude	Preferred Model
1.6 μT	6^{th} Order Combination
2.4 μT	5^{th} Order Combination
3.2 μT	4^{th} Order Combination
4.0 μT	3^{rd} Order Combination
All Amplitudes	6^{th} Order Combination

3.3 RESULTS FOR AIM 3: BLADDER CANCER IMAGES

3.3.1 CURVE FITTING RESULTS

The bladder cancer patient images were acquired with a 4.0 μT saturation amplitude. Data points were excluded when the signal intensity at a frequency offset fell below the

threshold of 5% of S_0, a procedure consistent with the exclusion procedure for the phantom data sets. Because of this, the 4th order combination was selected as the model for fitting the Z-spectra rather than the 3rd order combination model preferred for the prostate cancer patient images acquired with a 4.0 μT saturation amplitude.

A representative example of Z-spectra and the resulting curve fits are plotted for both the NBW and tumor regions in Figure 3.16. Generally, the points of the Z-spectra near water resonance for tumor regions fell beneath the exclusion threshold. The NBW regions typically had higher signal, and few data points were excluded from curve fitting. Seven patients had NBW Z-spectra that appeared noisy compared to the Z-spectra for other patients. A representative example of these Z-spectra and the resulting curve fits are plotted in Figure 3.17. This may be due to patient motion during the acquisition.

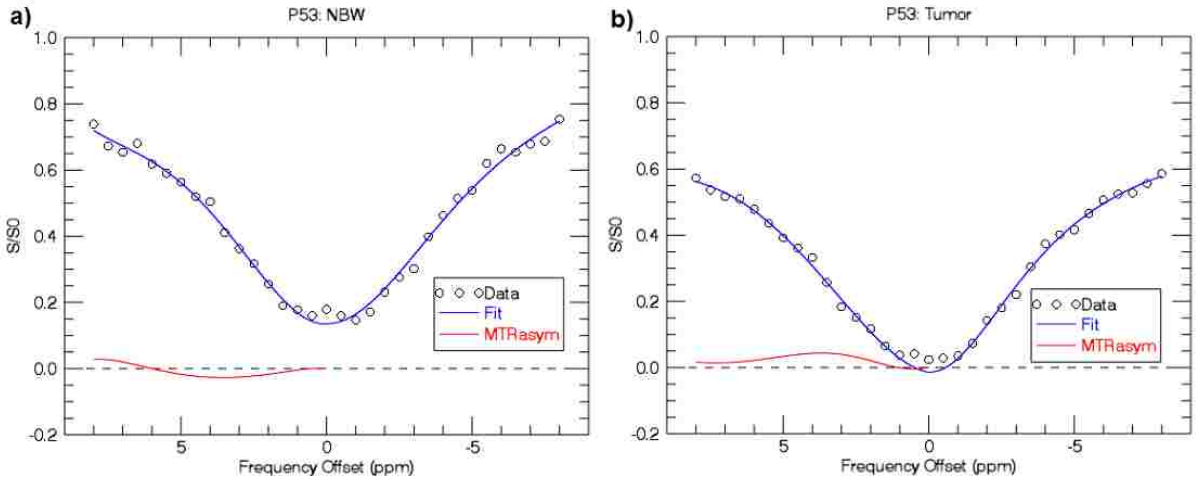

Figure 3.16: A representative example of Z-spectral curve fits and $MTR_{asym}(\omega)$ calculated from the interpolated Z-spectra for (a) the NBW region and (b) the tumor region of the bladder cancer patient images.

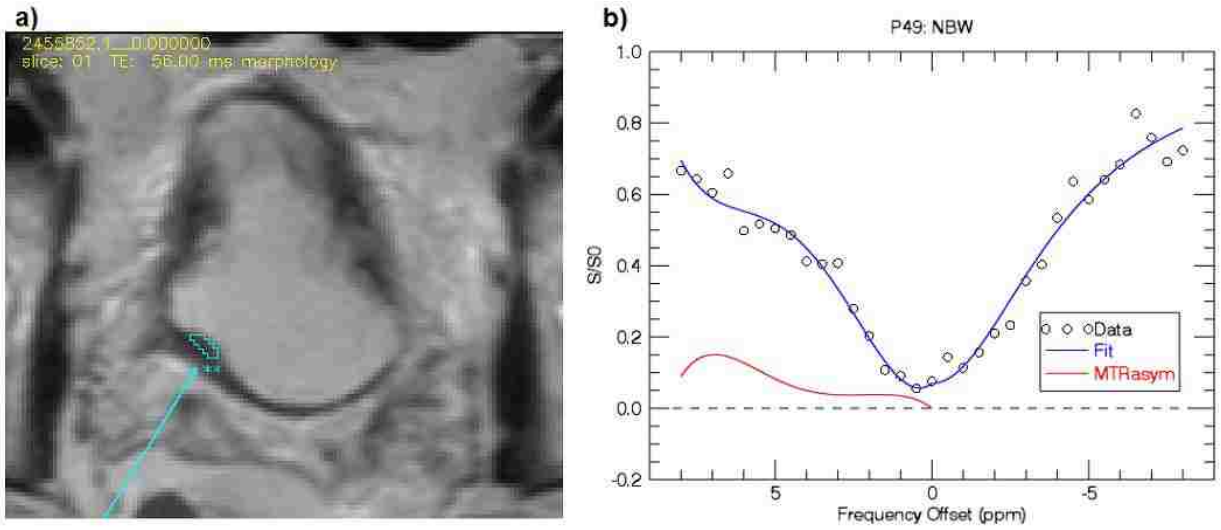

Figure 3.17: An example of (a) a small ROI for the NBW region, and (b) the Z-spectrum in that ROI for a patient who may have experienced bladder motion during acquisition.

3.3.2 BLADDER CANCER PATIENT MTR ASYMMETRY RESULTS

Using the Shapiro-Wilk test for normality on the distribution of MTR_{asym}(2.0 ppm) and MTR_{asym}(3.5 ppm) values in both the NBW and tumor regions, the null hypothesis of normality was unable to be rejected, enabling the use of the Student's *t*-test.

A paired statistically significant difference was found between the MTR_{asym}(3.5 ppm) quantities in the NBW and tumor regions ($p < 0.001$), while no significant difference ($p > 0.05$) was found between the MTR_{asym}(2.0 ppm) quantities between the NBW and tumor regions.

The average MTR_{asym}(3.5 ppm) value in NBW regions was -0.0119 ± 0.0478, while the average value in tumor regions was 0.0336 ± 0.0225 (Figure 3.17a). The average MTRasym(2.0 ppm) value in NBW regions was -0.0020 ± 0.0569, while the average value in tumor regions was 0.0176 ± 0.0222 (Figure 3.17b).

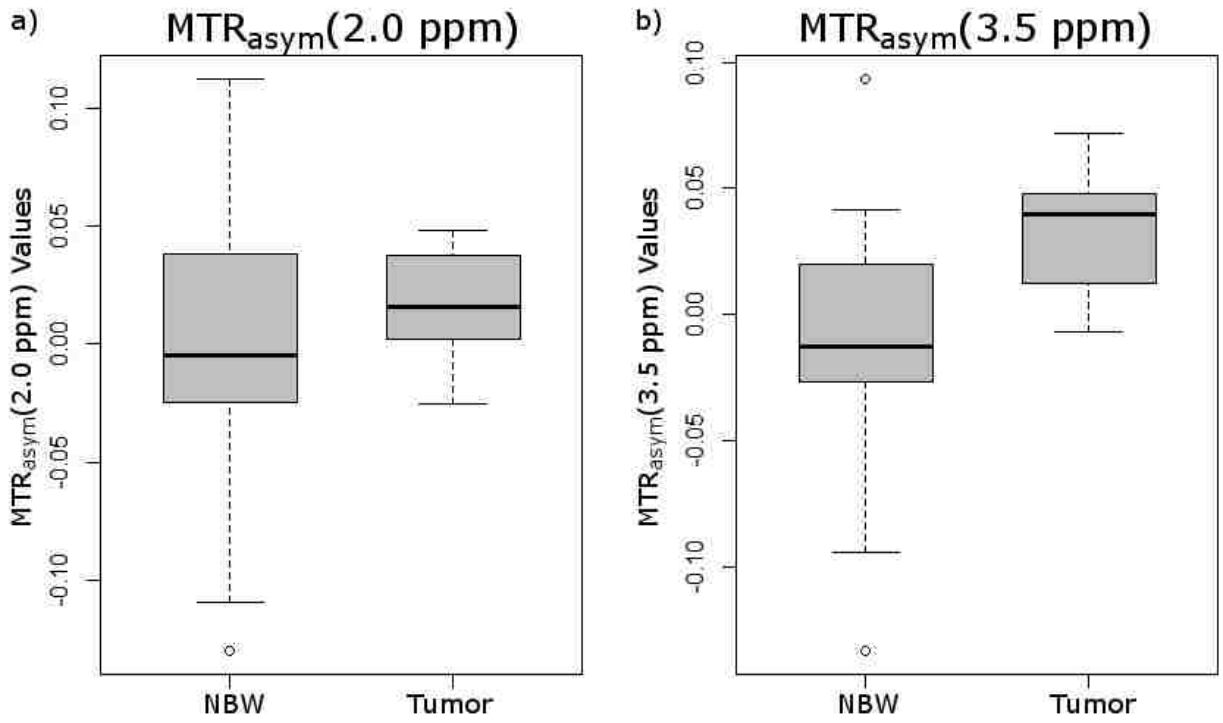

Figure 3.18: Boxplots of the distribution of (a) MTR_{asym}(2.0 ppm) values and (b) MTR_{asym}(3.5 ppm) values in both the NBW and tumor regions.

CHAPTER 4: DISCUSSION AND CONCLUSIONS

4.1 RESULTS SUMMARY

In this work, a Z-spectral curve fitting model was proposed which separated the components of the Z-spectrum upfield and downfield from water resonance during the fitting process. Reported methods of Z-spectral analysis relied on high order polynomials for interpolation, which were not based on the physics of CEST-MRI and were prone to exhibiting oscillations near the edge of the fitting interval under some circumstances. The model proposed in this work was partially based on the solution to the Bloch equations modified to account for the transfer of magnetization between pools of protons either associated with solutes, immobile macromolecules, or free water, and relies on lower order polynomials to fit half of the Z-spectrum. This method of fitting both provided some physically meaningful fitting parameters and reduced the magnitude of the oscillations. This method of fitting the upfield and downfield sections separately was shown to be preferred based on the AICc model selection criterion. The capability of MTR_{asym} calculations made using this model to distinguish tumor from healthy tissue was demonstrated for bladder cancer. The motivation for this work was the lack of a standard procedure for data processing in CEST-MRI studies, combined with a lack of a standard phantom for comparing results across MR systems.

It was hypothesized that a model which fit the regions of the Z-spectrum upfield and downfield from water separately would result in fits of similar quality as the high order polynomial functions reported in the literature while reducing the required number of fitting parameters, and thus maintaining the ability to calculate useful MTR_{asym} values. This was tested by first applying the models to a comprehensive CEST-MRI phantom and calculating the AICc for each to determine a preferred curve fitting model based on the minimum average AICc value.

A subset of these models was then applied to a set of prostate cancer patient images and again the preferred model was identified as the minimum average AICc. Finally, a model was selected from the phantom and prostate cancer results and applied to bladder cancer images; MTR_{asym}(2.0 ppm) and MTR_{asym}(3.5 ppm) values were calculated for both NBW and tumor regions to determine if these regions could be distinguished by differences in MTR asymmetry values.

For the phantom and prostate cancer patient images acquired at all saturation amplitudes, a combination model was preferred using a 5^{th} and 6^{th} order polynomial, respectively, to describe the downfield regions of the Z-spectra. A 4^{th} order combination fitting method was applied to bladder cancer patient images and the MTR_{asym}(3.5 ppm) calculations were found to be significantly different between NBW and tumor regions, demonstrating the ability of MTR_{asym}(3.5 ppm) calculations made using this model to distinguish NBW from tumor.

In addition to incorporating some physical meaning, this model has the potential to be extended further to include terms describing Z-spectral contributions from NOE which would make it suitable for application to CEST-MRI at ultra-high field strengths (greater than 3 T).

4.2 LIMITATIONS OF PROPOSED MODEL

The Lorentzian lineshape describing the effect of DWS in the combination upfield and downfield fitting method was based on the solution to modified Bloch equations under the assumption of weak saturation (Zhou, Wilson et al. 2004, Zaiß, Schmitt et al. 2011). In many experimental conditions, this assumption will not be satisfied as the water signal will be fully suppressed at saturation frequency offsets close to water resonance. This could result in large variances in MTR asymmetry calculations made in regions where the assumption of weak saturation fails.

As with all methods for interpolating Z-spectra for MTR asymmetry calculations, accurate B_0 field inhomogeneity maps are required to ensure accurate calculations. Methods which shift the Z-spectrum based on curve fitting results have the advantage of not requiring user input when selecting appropriate sequence parameters for acquiring B_0 field inhomogeneity maps. Figure 3.1 demonstrates variation in B_0 field inhomogeneity measurements made using the same technique with differences in echo time separation. It has been shown that B_0 inhomogeneities as small as 0.1 ppm can significantly affect the asymmetry calculations (Kim, Gillen et al. 2009).

Separating the curve fitting process into two parts takes additional time to process. While not problematic when fitting ROIs, the extra time may become an issue if the technique was applied on a per-pixel basis. Processing multiple slices per image data set will add even more time.

The present study only assesses the MTR_{asym} values calculated using a single instance of the combination model. This offers no basis for comparing the results of the high order polynomial models reported in the literature to the results of the combination model.

4.3 AIM 1, DISCUSSION

Eight fitting models were applied to 84 data sets. Average AICc was calculated for each model, with the models then ranked from the most negative average AICc to the largest average AICc value. The 20^{th} order polynomial model ranked last in 79 of the 84 data sets tested, and ranked next to last for the remaining 5 data sets. Although the 20^{th} order polynomial had the lowest residual sum of squares for every data set, it consistently had the largest average AICc because of the large ratio of fitting parameters to data points.

At lower saturation amplitudes, the combination model with low order polynomials for the downfield region of the Z-spectra generally performed poorly based on the AICc model selection criteria, which was the result of the low order polynomial being unable to fit the sharper curve in the Z-spectra. This contrasted with the 20^{th} order polynomial which appeared to fit the data well but was heavily penalized by the AICc for having many fitting parameters. Increasing the saturation amplitude both increased the width of the DWS component of the Z-spectra and increased the magnitude of the MT component (Zaiß, Schmitt et al. 2011), resulting in the shoulders of the Z-spectra being less pronounced; this enabled the lower order polynomials to perform better for the combination model. The 20^{th} order polynomial fitting clearly exhibited oscillations near the edges of the fitting intervals with the higher saturation amplitudes.

Near 0 ppm, where data points were excluded from the fitting process due to falling beneath a threshold of signal of 5% of S_0, the assumption of weak saturation failed. The saturation amplitudes were chosen to reflect values that have been used in past experiments *in vivo* (Jia, Abaza et al. 2011). In the future, imaging with a lower saturation amplitude may be preferable to increase the number of data points for which the weak saturation approximation is applicable. The performance of the 20^{th} order polynomial model suffered due to this exclusion of data points during the curve fitting process, effectively increasing the ratio of the number of fitting parameters to the number of data points.

4.4 AIM 2, DISCUSSION

Six fitting models were applied to 232 Z-spectral data sets acquired from the prostate cancer patient images. Similar to the phantom results, the 20^{th} order polynomial model had the greatest average AICc values over all data sets despite having the least residual sum of squares values for all data sets.

As with the phantom results, the combination models were the preferred curve fitting models. The order of the polynomial used to fit the downfield region of the Z-spectra decreased with increasing saturation amplitude. This was due to the increase in the MT effect as well as the broadening of the DWS component of the Z-spectra, as referenced in the previous section. At lower saturation amplitudes, the 3rd and 4th order polynomials used for the combination model did not adequately fit the Z-spectra. At higher saturation amplitudes, the combination models using 3rd and 4th order polynomials were preferred based on having smaller average AICc values.

For the Z-spectral data from prostate cancer patient images, data points near the center of the Z-spectra were not excluded because of previous experience with these data sets indicating that this would not be necessary to achieve good fitting (Schurr, Elias et al. 2014). This previous study applied Equation 2.1 to the full set of Z-spectral data. Although regions in the center of the Z-spectrum were close to the exclusion threshold applied to the phantom Z-spectra, the quality of the fitting was still good based on the average AICc values used for the preferred model selection.

4.5 AIM 3, DISCUSSION

The 4th order combination model was applied to the bladder cancer patients because this had the most negative average AICc values for the phantom at a saturation amplitude of 4.0 μT, which was the saturation amplitude used during the acquisition of the bladder cancer patient images. The curve fitting procedure in the bladder followed the same exclusion process as in the phantom. For this reason, the preferred 4th order combination model from the phantom study was selected over the preferred 3rd order combination model from the prostate cancer patient study.

The MTR_{asym}(3.5 ppm) values were statistically significantly greater in the tumor regions than the NBW regions, which showed that this quantity has the potential to distinguish these

regions. The MTR_{asym}(2.0 ppm) values were not statistically significantly different between the two regions, but this potentially was due to the large saturation amplitude used in the experiment. The signal intensity at a frequency offset of ±2.0 ppm was very close to the exclusion threshold for many of the Z-spectra. Repeating the experiment with a reduced saturation amplitude may yield different results.

The Z-spectra collected in the NBW regions for some patients did not have the smooth Z-spectral shape as shown for the phantom or prostate cancer patient images. This was likely due to bladder motion during the imaging procedure. For frequency offsets far from water resonance, the ROI can be adjusted to account for motion; however, at frequency offsets close to water resonance there is low signal and it is not always possible to account for motion. The ROIs for the NBW regions were very small, and the boundaries of the bladder wall were not always clear in the CEST-MR images. Though to date there have been no studies on CEST-MRI of bladder cancer published and indexed in the PubMed database, the quantity MTR_{asym}(3.5 ppm) has been shown in studies of other sites to have the ability to distinguish disease from healthy tissue (Jia, Abaza et al. 2011).

4.6 DIRECTION OF FUTURE WORK

Future work on this fitting model may need to constrain the slopes of the fits in the upfield and downfield regions to match at the origin to prevent artifacts in MTR asymmetry calculations at saturation frequency offsets close to water resonance. This will become more important at lower saturation amplitudes, or for imaging solutes which exhibit a CEST effect near water resonance such as glycogen. Eventually, the combination model for curve fitting could be written into a standalone image processing software and made available for use by the community.

Establishing MTR_{asym} calculations as a clinically relevant quantitative imaging biomarker will require additional work to establish the scan-rescan and cross-system reproducibility. A standard CEST-MRI phantom will be useful for this process, and the phantom used in this study could be modified for this role. The size of the phantom should be reduced to enable it to fit in smaller detector coils. Changing the temperature or pH of the phantoms may be useful as well.

If new terms were added to the fitting model to account for NOE, the model could be applied to CEST-MRI at ultra-high field strengths. Many CEST-MRI studies are performed at field strengths greater than 3 T, and adapting the model to apply to these conditions would increase the number of studies for which the model would be relevant.

The bladder cancer study could be extended to include patient images from follow-up MR scans. For patients undergoing chemotherapy for instance, one could assess changes in MTR_{asym} in response to therapy. Another venue is to assess whether MTR_{asym} can predict a patient's response to chemotherapy.

In conclusion, the Z-spectral analysis method proposed in this study of fitting the upfield and downfield regions of the Z-spectrum separately provided a better model than some higher order polynomial models reported in the literature, according to the AICc model selection criteria. This was demonstrated in both phantom and patient images using multiple amplitudes for the saturation pre-pulse. Additionally, the model provided a model based in part on the physics of MT-MRI and CEST-MRI. The application of the model to bladder cancer patients demonstrated that the MTR_{asym}(3.5 ppm) calculations performed using the combination can provide quantitative methods of distinguishing NBW from bladder cancer, a site which has not been previously studied by with CEST-MRI.

REFERENCES

Arima, K., N. Hayashi, M. Yanagawa, J. Kawamura, S. Kobayashi, K. Takeda and Y. Sugimura (1999). "The progress in diagnostic imaging for staging of bladder and prostate cancer: endorectal magnetic resonance imaging and magnetization transfer contrast." Hinyokika kiyo. Acta urologica Japonica **45**(8): 553-557.

Bryant, R. G. (1996). "The dynamics of water-protein interactions." Ann Rev Bioph Biom **25**: 29-53.

Chen, C. Y., C. W. Li, Y. T. Kuo, T. S. Jaw, D. K. Wu, J. C. Jao, J. S. Hsu and G. C. Liu (2006). "Early Response of Hepatocellular Carcinoma to Transcatheter Arterial Chemoembolization: Choline Levels and MR Diffusion Constants—Initial Experience." Radiol **239**(2): 448-456.

Desmond, K. L. and G. J. Stanisz (2012). "Understanding quantitative pulsed CEST in the presence of MT." Magn Reson Med **67**(4): 979-990.

Dula, A. N., L. R. Arlinghaus, R. D. Dortch, B. E. Dewey, J. G. Whisenant, G. D. Ayers, T. E. Yankeelov and S. A. Smith (2013). "Amide proton transfer imaging of the breast at 3 T: establishing reproducibility and possible feasibility assessing chemotherapy response." Magn Reson Med **70**(1): 216-224.

Green, D. A., M. Durand, N. Gumpeni, M. Rink, E. K. Cha, P. I. Karakiewicz, D. S. Scherr and S. F. Shariat (2012). "Role of magnetic resonance imaging in bladder cancer: current status and emerging techniques." Brit J Urol **110**(10): 1463-1470.

Haacke, E. M., R. W. Brown, M. R. Thompson and R. Venkatesan (1999). Magnetic Resonance Imaging: Physical Principles and Sequence Design. New York, John Wiley & Sons, Inc.

Hattori, K., Y. Ikemoto, W. Takao, S. Ohno, T. Harimoto, S. Kanazawa, M. Oita, K. Shibuya, M. Kuroda and H. Kato (2013). "Development of MRI phantom equivalent to human tissues for 3.0-T MRI." Med Phys **40**(3): 11.

Henkelman, R. M., X. M. Huang, Q. S. Xiang, G. J. Stanisz, S. D. Swanson and M. J. Bronskill (1993). "Quantitative interpretation of magnetization-transfer." Magn Reson Med **29**(6): 759-766.

Henkelman, R. M., G. J. Stanisz and S. J. Graham (2001). "Magnetization transfer in MRI: a review." NMR Biomed **14**(2): 57-64.

Hoeks, C. M. A., J. O. Barentsz, T. Hambrock, D. Yakar, D. M. Somford, S. W. T. P. J. Heijmink, T. W. J. Scheenen, P. C. Vos, H. Huisman, I. M. van Oort, J. A. Witjes, A. Heerschap and J. J. Fütterer (2011). "Prostate Cancer: Multiparametric MR Imaging for Detection, Localization, and Staging." Radiol **261**(1): 46-66.

Hurvich, C. M. and C. L. Tsai (1989). "Regression and Time Series Model Selection in Small Samples." Biometrika **76**(2): 297-307.

Jia, G., R. Abaza, J. D. Williams, D. L. Zynger, J. Y. Zhou, Z. K. Shah, M. Patel, S. Sammet, L. Wei, R. R. Bahnson and M. V. Knopp (2011). "Amide Proton Transfer MR Imaging of Prostate Cancer: A Preliminary Study." J Magn Reson Im **33**(3): 647-654.

Kim, M., J. Gillen, B. A. Landman, J. Zhou and P. C. van Zijl (2009). "Water saturation shift referencing (WASSR) for chemical exchange saturation transfer (CEST) experiments." Magn Reson Med **61**(6): 1441-1450.

Kogan, F., H. Hariharan and R. Reddy (2013). "Chemical Exchange Saturation Transfer (CEST) Imaging: Description of Technique and Potential Clinical Applications." Curr Radiol Rep **1**(2): 102-114.

Kogan, F., M. Haris, C. Debrosse, A. Singh, R. P. Nanga, K. Cai, H. Hariharan and R. Reddy (2014). "In vivo chemical exchange saturation transfer imaging of creatine (CrCEST) in skeletal muscle at 3T." J Magn Reson Im **40**(3): 596-602.

Kogan, F., M. Haris, A. Singh, K. Cai, C. Debrosse, R. P. Nanga, H. Hariharan and R. Reddy (2014). "Method for high-resolution imaging of creatine in vivo using chemical exchange saturation transfer." Magn Reson Med **71**(1): 164-172.

Kumar, V., N. R. Jagannathan, R. Kumar, S. Thulkar, S. D. Gupta, A. K. Hemal and N. P. Gupta (2008). "Evaluation of the role of magnetization transfer imaging in prostate: a preliminary study." Magn Reson Imag **26**(5): 644-649.

Kumar, V., N. R. Jagannathan, S. Thulkar and R. Kumar (2012). "Prebiopsy magnetic resonance spectroscopy and imaging in the diagnosis of prostate cancer." Int J Urol **19**(7): 602-613.

Langer, D. L., T. H. van der Kwast, A. J. Evans, J. Trachtenberg, B. C. Wilson and M. A. Haider (2009). "Prostate Cancer Detection With Multi-parametric MRI: Logistic Regression Analysis of Quantitative T2, Diffusion-Weighted Imaging, and Dynamic Contrast-Enhanced MRI." J Magn Reson Im **30**(2): 327-334.

Liu, G., X. Song, K. W. Chan and M. T. McMahon (2013). "Nuts and bolts of chemical exchange saturation transfer MRI." NMR Biomed **26**(7): 810-828.

Markwardt, C. B. (2009). "Non-Linear Least Squares Fitting in IDL with MPFIT." ADASS XVIII, Quebec, Canada, Astronomical Society of the Pacific: San Fransisco.

Martens, M. H., D. M. Lambregts, N. Papanikolaou, L. A. Heijnen, R. G. Riedl, A. zur Hausen, M. Maas, G. L. Beets and R. G. Beets-Tan (2014). "Magnetization transfer ratio: a potential biomarker for the assessment of postradiation fibrosis in patients with rectal cancer." Invest Radiol **49**(1): 29-34.

Mehta, R. C., G. B. Pike and D. R. Enzmann (1995). "Improved detection of enhancing and nonenhancing lesions of multiple-sclerosis with magnetization-transfer." Am J Neuroradiol **16**(9): 1771-1778.

Morrison, C. and R. M. Henkelman (1995). "A model for magnetization-transfer in tissues." Magn Reson Med **33**(4): 475-482.

Nguyen, H. T., G. Jia, Z. K. Shah, K. Pohar, A. Mortazavi, D. L. Zynger, L. Wei, X. Yang, D. Clark and M. V. Knopp (2015). "Prediction of chemotherapeutic response in bladder cancer using K-means clustering of dynamic contrast-enhanced (DCE)-MRI pharmacokinetic parameters." J Magn Reson Im **41**(5): 1374-1382.

Parker, D. L., H. R. Buswell, K. C. Goodrich, A. L. Alexander, N. Keck and J. S. Tsuruda (1995). "The application of magnetization-transfer to MR-angiography with reduced total power." Magn Reson Med **34**(2): 283-286.

Pazahr, S., I. Blume, P. Frei, N. Chuck, D. Nanz, G. Rogler, M. Patak and A. Boss (2013). "Magnetization transfer for the assessment of bowel fibrosis in patients with Crohn's disease: initial experience." Magma **26**(3): 291-301.

R Development Core Team (2014). R: A language and environment for statistical computing. Vienna, Austria, R Foundation for Statistical Computing.

Riches, S. M., V. A.; Collins, D. J.; Giles, S.; deSouza, N. M. (2009). "Evaluating prognostic biomarkers of prostate cancer behaviour: use of magnetization transfer and diffusion weighted contrast." ISMRM 17th Annual Scientific Meeting & Exhibition. Honolulu, HI.

Schurr, R. N., S. N. Elias, W. Wei, J. Keupp, M. V. Knopp, G. Jia and S. B. Heymsfield (2014). A Two-Pool Modeling for 3 Tesla Magnetization Transfer MR Imaging of Prostate Cancer. RSNA 2015 Scientific Assembly and Annual Meeting. Chicago, IL.

Siegel, R. L., K. D. Miller and A. Jemal (2015). "Cancer Statistics, 2015." Ca-cancer J Clin **65**(1): 5-29.

Singh, A., M. Haris, K. Cai, V. B. Kassey, F. Kogan, D. Reddy, H. Hariharan and R. Reddy (2012). "Chemical exchange saturation transfer magnetic resonance imaging of human knee cartilage at 3 T and 7 T." Magn Reson Med **68**(2): 588-594.

Sun, P. Z. (2010). "Simplified and scalable numerical solution for describing multi-pool chemical exchange saturation transfer (CEST) MRI contrast." J Magn Reson **205**(2): 235-241.

Taylor, R., I. Magnusson, D. L. Rothman, G. W. Cline, A. Caumo, C. Cobelli and G. I. Shulman (1996). "Direct assessment of liver glycogen storage by 13C nuclear magnetic resonance spectroscopy and regulation of glucose homeostasis after a mixed meal in normal subjects." J Clin Invest **97**(1): 126-132.

Tozer, D., A. Ramani, G. J. Barker, G. R. Davies, D. H. Miller and P. S. Tofts (2003). "Quantitative magnetization transfer mapping of bound protons in multiple sclerosis." Magn Reson Med **50**(1): 83-91.

van Zijl, P. C., C. K. Jones, J. Ren, C. R. Malloy and A. D. Sherry (2007). "MRI detection of glycogen in vivo by using chemical exchange saturation transfer imaging (glycoCEST)." Proc Natl Acad Sci U S A **104**(11): 4359-4364.

Ward, K. M., A. H. Aletras and R. S. Balaban (2000). "A New Class of Contrast Agents for MRI Based on Proton Chemical Exchange Dependent Saturation Transfer (CEST)." J Magn Reson Im **143**(1): 79-87.

Wei, W., G. Jia, D. Flanigan, J. Zhou and M. V. Knopp (2014). "Chemical exchange saturation transfer MR imaging of articular cartilage glycosaminoglycans at 3 T: Accuracy of B0 Field Inhomogeneity corrections with gradient echo method." Magn Reson Imaging **32**(1): 41-47.

Westbrook, C., C. K. Roth and J. Talbot (2011). MRI in Practice. West Sussex, Wiley-Blackwell.

Yadav, N. N., K. W. Chan, C. K. Jones, M. T. McMahon and P. C. van Zijl (2013). "Time domain removal of irrelevant magnetization in chemical exchange saturation transfer Z-spectra." Magn Reson Med **70**(2): 547-555.

Zaiss, M. and P. Bachert (2013). "Chemical exchange saturation transfer (CEST) and MR Z-spectroscopy in vivo: a review of theoretical approaches and methods." Phys Med Biol **58**(22): R221-269.

Zaiß, M., B. Schmitt and P. Bachert (2011). "Quantitative separation of CEST effect from magnetization transfer and spillover effects by Lorentzian-line-fit analysis of z-spectra." J Magn Reson Im **211**(2): 149-155.

Zhou, J., J. F. Payen, D. A. Wilson, R. J. Traystman and P. C. M. van Zijl (2003). "Using the amide proton signals of intracellular proteins and peptides to detect pH effects in MRI." Nat Med **9**(8): 1085-1090.

Zhou, J. and P. C. M. van Zijl (2006). "Chemical exchange saturation transfer imaging and spectroscopy." Prog Nucl Magn Reson Spectrosc **48**(2–3): 109-136.

Zhou, J., D. A. Wilson, P. Z. Sun, J. A. Klaus and P. C. Van Zijl (2004). "Quantitative description of proton exchange processes between water and endogenous and exogenous agents for WEX, CEST, and APT experiments." Magn Reson Med **51**(5): 945-952.

Ziv, K. and S. S. Gambhir (2013). "Bioengineering and regenerative medicine: Keeping track." Nat Mater **12**(3): 180-181.

VITA

Ryan Nicholas Schurr, a native of Tampa, Florida, received his bachelor's degree at Clemson University in 2012. Thereafter, he entered graduate school in the Department of Physics and Astronomy at Louisiana State University. He is a candidate to receive his master's degree in 2015 and plans to begin a residency for radiation physics at Scott & White Memorial Hospital in Temple, Texas, following graduation.